Reviews in Mineralogy & Geochemistry
Vol. 63, pp. 363-397, 2006

Small-Angle Neutron Scattering and the Microstructure of Rocks

Andrzej P. Radlinski

Geoscience Australia
GPO Box 378,
Canberra City, Australian Capital Territory 2601, Australia
e-mail: Andrzej.Radlinski@ga.gov.au

INTRODUCTION

The self-similarity of rocks on the macro-scale is well known—traditionally, the photographs of rock formations usually include a scale-defining object such as a coin, a hammer, a human silhouette, etc. We know now that rock self-similarity, expressed in the quantitative language of fractal geometry, is also ubiquitous in the micro-world as well. In fact, sedimentary rocks are some of the most extensive microstructural fractal systems found in nature. Much of the knowledge of self-similarity on the micro-scale has been accumulated over the last two decades using small-angle neutron scattering (SANS) and small-angle X-ray scattering (SAXS).

In the family of neutron scattering techniques, small-angle scattering has the lowest spatial resolution (Vogel and Priesmeyer 2006, this volume)—it cannot detect the position of individual atoms. It can, however (using two different experimental designs), explore the internal micro-architecture of the pore space over an impressive linear scale range (from nanometers to tens of micrometers). The technique is non-invasive and gives an average value for a given sample volume.

In the following, it is demonstrated how SANS can be used to explore the microstructure of sedimentary and igneous rocks and help gain insights into internal specific surface area, porosity, pore size distribution, mercury intrusion porosimetry, compaction, subsurface generation of oil and gas, adsorption of gases, imbibition of water, distribution of crystalline precipitates and the microstructural effects of heat treatment.

It is the author's intention to provide both a comprehensive introduction for newcomers to the subject and a reference text for those already familiar with small-angle scattering techniques. The article includes a review of theoretical results, selected examples, description of experimental procedures, examples of interpreted data for various types of rocks and references to original work.

BACKGROUND

Small-angle scattering (SAS) techniques

SANS (Small-Angle Neutron Scattering) and SAXS (Small-Angle X-ray Scattering), have been used for decades to study the geometry of supra-molecular objects. These objects can be suspended in solvents or aggregated into a solid phase. With modern small-angle scattering apparatus the size of objects accessible with SANS and SAXS extends from approximately 1 nm to 20 μm. There is an extensive literature on the theory and practice of SAS (for a review see Guinier et al. 1955; Glatter and Kratky 1982; Feigin and Svergun 1989; Espinat 1990; Lindner and Zemb 1991).

1529-6466/06/0063-0014$05.00 DOI: 10.2138/rmg.2006.63.14

SANS and SAXS are very similar techniques. There are subtle practical reasons for neutrons being, in general, more suitable for microstructural work on sedimentary rocks rather than X-rays. In the following, the emphasis is on SANS, but some examples of SAXS work are also given.

Rocks as natural fractal systems

Although geological samples (particularly coals) have been studied by SAXS since the 1930's, the advent of fractal geometry (Mandelbrot 1977, 1982) brought about unprecedented developments when the connection was made between fractals and the microstructure of heterogeneous surfaces (Pfeifer and Avnir 1983). Katz and Thompson (1985) used SEM and optical microscopy to demonstrate the fractal character of pore space in sandstones over length scales ranging from 0.1 to 100 μm. This was followed by a series of papers on the microstructure of shales, sandstones and carbonates, which established that the upper size limit for fractal behavior ranges from 5 to 100 μm (depending on rock lithology) (Krohn 1988, Thompson 1991). Other studies of fractal features of sandstone and limestone rocks include the works of Jacquin and Adler (1987) and Hansen and Skjeltrop (1988), who used optical microscopy to determine fractal volume and surface dimensions.

The discovery of the fractality of rock microstructure provided fresh impetus for SAS work. Bale and Schmidt (1984) derived the analytical form of the correlation function for surface fractals (micron-sized pores with fractal boundary surfaces) and applied it to the analysis of SAXS power law scattering data obtained for lignite coals. The expression for the correlation function was later refined by Mildner and Hall (1986) to account for the limited size of fractal objects and by Wong and Bray (1988) to explain finite scattering as the fractal dimension approaches the value of 3. Wong et al. (1986) used SANS to study the microstructure of sandstone, shale, limestone and dolomite samples over scales of 5 to 500 Å. They found non-universal power-law scattering—indicating the surfaces of sandstones and shales are fractal (which they attributed to varying clay content in the samples). Inspired by the unique microstructural properties of sedimentary rocks, Cohen (1987) presented a general theoretical model of various morphological regimes in sedimentary rocks. He attributed suppressed grain sintering and the formation of a rough grain-pore interface to a small pore-grain free energy in comparison to the grain boundary free energy, and pointed to the anti-sintering thermodynamic regime as the source of ubiquitous fractality of the pore-rock interface.

Geological applications of SAS

In the following decade, small-angle scattering techniques were integrated into mainstream petroleum geology and engineering (Radlinski et al. 1996a, 1999, 2000a, 2004a,b; Boreham et al. 2003) and coal geology (Reich et al. 1990; Radlinski and Radlinska 1999; McMahon et al. 2002; Prinz et al. 2004; Radlinski et al. 2004c). SAS research into various aspects of the microstructure of porous media, including rocks, has continued (e.g., Allen 1991; Broseta et al. 2001; Spalla et al. 2003), and there has been increased interest in the microstructure of igneous rocks (Lucido et al. 1988; Floriano et al. 1994; Kahle et al. 2004; Winkler et al. 2005).

Principle of SAS experiments

The principle of a pinhole SANS experiment is illustrated in Figure 1. A flux of monochromatic thermal neutrons propagating in the direction of their wavevector $\mathbf{k_0}$ is elastically scattered inside a sample of uniform thickness t and irradiated volume V. The magnitude of $\mathbf{k_0}$ is λ^{-1}, where λ is the neutron wavelength. One measures intensity dI scattered in direction $\mathbf{k}$, where by convention $\mathbf{k} - \mathbf{k_0} = \mathbf{s}$ and the quantity $\mathbf{Q} = 2\pi\mathbf{s}$ is called the scattering vector. It follows from Figure 1 that the magnitude of $\mathbf{s}$ is $2\sin\Theta/\lambda$. The magnitude of the scattering vector is thus related to neutron wavelength λ and the scattering angle 2θ by $Q = (4\pi/\lambda)\sin\theta$.

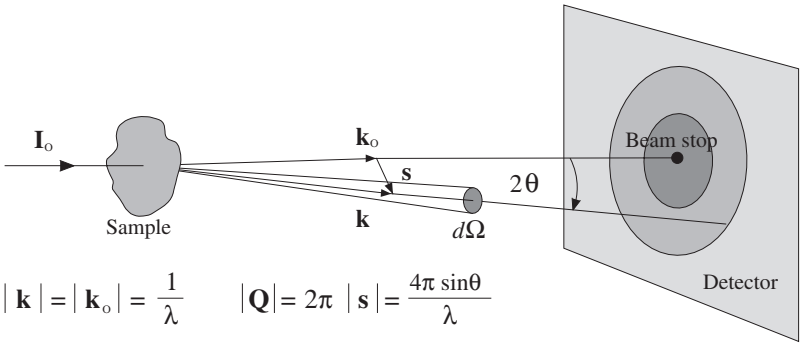

Figure 1. The principle of a pinhole SANS experiment.

The incident flux of the scattering radiation (particles) is denoted by Φ_0, i.e., $\Phi_0 = I_0/A$, where I_0 is the incident intensity (neutrons per second) and A is the beam cross sectional area at the sample position (Fig. 1). The scattered intensity monitored in the solid angle element $d\Omega$ targeted by the scattering vector **Q** can be expressed as

$$dI \propto \Phi_0 \frac{d\sigma}{d\Omega} d\Omega \tag{1}$$

where $d\sigma$ is the elemental scattering cross section. The quantity $d\sigma/d\Omega$ is called the differential cross section of scattering. It is the purpose of SAS experiment to measure $d\sigma/d\Omega$ in absolute units.

Scale range accessible using SANS and USANS instruments

The Bragg formula for diffraction, $\lambda = 2d \sin\theta$, shows that for a fixed λ, the angle of diffraction, θ, varies inversely with the distance between the diffracting lattice planes, d. For inorganic crystals, d and λ (for both X-rays and neutrons) are of the same order of magnitude (several Å) and the scattering angles are large. For materials with non-periodic structure, one is often interested in large-scale features (of the order of magnitude from tens of angstroms to a fraction of a millimeter). This requires acquisition of experimental data at small scattering angles.

The linear size of objects that contribute most to the scattering at a given Q-value is of the order of $1/Q$. For periodic structures the size is given by $2\pi/Q = \lambda/(2\sin\theta)$—it is another form of the Bragg law. For fractal (widely polydisperse non-periodic) systems, the size is approximately $2.5/Q \approx 0.4\lambda/(2\sin\theta)$ (Radlinski et al. 2000a). Thus, the precise linear size range accessible with SANS can be selected by choosing neutron wavelength λ and the range of the scattering angles. SANS and SAXS instruments are designed to maximize the Q-range and to minimize parasitic contributions to the scattering signal.

A SANS experiment is performed in a transmission geometry and measures the intensity of radiation scattered at angles very close to the direction of propagation of the incident beam. As the upper limit of 2θ in a SANS experiment is about 5°, it follows that $\sin\theta \approx \theta$ and Q is simply a measure of the scattering angle in units of $Å^{-1}$. A typical range of neutron wavelengths available for a SANS experiment is 4 – 20 Å.

The relationship between the scattering angle 2θ, scattering vector Q, and the linear size of objects accessible with various small-angle scattering instruments for two wavelengths (1.5 Å - close to wavelengths used in USANS and SAXS instruments, and 4 Å - close to the flux maximum for SANS instruments) is illustrated in Figure 2. At the smallest linear scales, Bragg

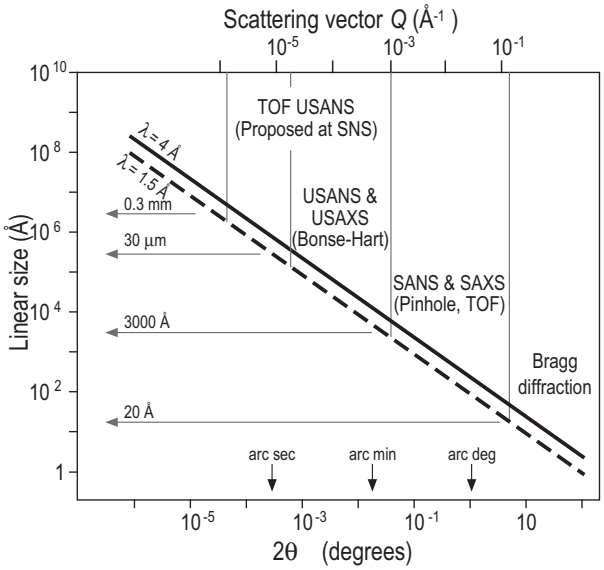

Figure 2. Linear scale range accessible with SANS and SAXS techniques. Q-values are calculated for $\lambda = 4$ Å.

diffraction covers the 2θ range from about 5° to nearly 180° (which corresponds to linear size range of about 1-20 Å). The angular range $4' < 2\theta < 5°$ (Q-range 10^{-1} to 10^{-3} Å^{-1}) is the traditional SANS (and SAXS) domain. This corresponds to the linear size range 20-3000 Å. Two types of SANS instruments (reactor based pinhole, e.g., Koehler 1986, Glinka et al. 1986, Lindner et al. 1992 and spallation source based time-of-flight, e.g., Thiyagarajan et al. 1997), operate in this range.

For the ultra-small angle (USANS and USAXS) region, where the scattering angles are in the range $6'' < 2\theta < 5'$ (Q-range 10^{-3} to 10^{-5} Å^{-1}) and the linear size ranges from 3000 Å to 30 μm, resolution of the incident and scattered beam is achieved by collimating and analyzing the beam using multiple reflections from perfect silicon crystals (Bonse and Hart 1965; Lambard and Zemb 1991; Agamalian et al. 1997; Hainbuchner et al. 2000). Practical USANS machines were developed only recently (Agamalian et al. 1997) and they have proved very useful in microstructural studies of geological materials (Radlinski et al. 1999, 2004a,b,c). There are several types of Bonse-Hart instruments—some have an option to sacrifice resolution for data acquisition speed (Mikula et al. 1988; McMahon and Treimer 1998). There is a proposal to construct a powerful TOF USANS instrument at the SNS facility in Oak Ridge, which theoretically could reach the minimum Q-value of nearly 10^{-6} Å^{-1} (linear size of 0.3 mm).

SUMMARY OF THEORETICAL RESULTS

Correlation function

The central concept in small-angle scattering is correlation function, $\gamma(r)$. For disordered (random) materials it plays the same role as the lattice structure in crystals. Following the notation of Debye and Bueche (1949) and Debye et al. (1957), the correlation function is defined as

$$\gamma(\boldsymbol{r}) \langle\eta^2\rangle_{Av} = \langle\eta_A\eta_B\rangle_{Av} \quad (2)$$

where η_A, η_B are the local fluctuations in the physical property (dielectric constant for light,

electronic density for X-rays, nuclear scattering length for neutrons) that provides a scattering contrast from some average value at points A and B a distance **r** apart; $<\eta^2>_{Av}$ is the average value of η^2. Defined as such, $\gamma(\mathbf{r})$ is confined within the limits $0 = \gamma(\infty) < \gamma(\mathbf{r}) < \gamma(0) = 1$.

According to the classical theory of scattering (Guinier and Fournet 1955), the intensity scattered by a unit volume is given by the integral:

$$I(Q) = \iint < \eta_A \eta_B >_{Av} \exp(ik\mathbf{sr}) d\tau_A d\tau_B \tag{3}$$

where **s** is the vector difference between unit vectors pointing in the direction **k** and $\mathbf{k_0}$, respectively, $|\mathbf{s}| = 2\sin\Theta$, $k = 2\pi/\lambda$ and $\mathbf{Q} = k\mathbf{s}$. Therefore

$$I(Q) = < \eta^2 >_{Av} \int \gamma(\mathbf{r}) \exp(i\mathbf{Qr}) d\tau \tag{4}$$

For isotropic media, where $\gamma(\mathbf{r})$ depends on the absolute value of **r** only and not on its direction, one gets:

$$I(Q) = 4\pi < \eta^2 >_{Av} \int_0^\infty r^2 \gamma(r) \frac{\sin(Qr)}{Qr} dr \tag{5}$$

This relationship shows that the scattering intensity within the entire *Q*-range is determined by Fourier transform of the correlation function. Conversely, the correlation function can be calculated by the inverse Fourier transform if the scattering intensity is known within a wide enough *Q*-range. At the heuristic level, Equations (4) and (5) indicate that the microstructural information accessible via the small-angle scattering technique is determined by the information content inherent in the correlation function.

Two phase approximation

For a wide range of substances, the SAS data for geological materials and porous media can generally be interpreted accurately using a two-phase approximation. In this approximation, the scattering volume is viewed as comprised of supra-molecular-size regions, each characterized by one of two possible values of the physical property that provides the scattering contrast. For instance, for porous media these two regions are the solid matrix and the pore space, respectively.

Two phase approximation is a simplification inherent in the SAS method and has been implicitly or explicitly employed for many years. Following Adler et al. (1990), one can describe a two phase (porous) medium in terms of a binary phase function $Z(\mathbf{x})$, where $Z(\mathbf{x}) = 1$ if **x** points to void and $Z(\mathbf{x}) = 0$ if **x** points to solid matrix. First two moments of $Z(\mathbf{x})$ yield the porosity, $\Phi = <Z(\mathbf{x})>$, and the correlation function:

$$\gamma(\mathbf{r}) = \frac{< Z(\boldsymbol{x}) Z(\mathbf{x}+\mathbf{r}) - \Phi^2 >}{\Phi(1-\Phi)} \tag{6}$$

Equation (5) can now be written as

$$I(Q) = 4\pi(\Delta\rho)^2 \Phi(1-\Phi) \int_0^\infty r^2 \gamma(r) \frac{\sin(Qr)}{Qr} dr \tag{7}$$

where $(\Delta\rho)^2$ is the scattering contrast. Contrast calculations are discussed in detail in the following section. The correlation function can be expressed as the inverse Fourier transform of the scattering intensity data:

$$\gamma(\mathbf{r}) = \left[2\pi^2 (\Delta\rho)^2 \Phi(1-\Phi) \right]^{-1} \int_0^\infty Q^2 I(Q) \frac{\sin(Qr)}{Qr} dQ \tag{8}$$

Finally, the porosity Φ can be calculated from the invariant Q_{inv} (Porod 1952), defined as follows:

$$Q_{inv} = \int_0^\infty Q^2 I(Q)\ dQ = 2\pi^2 (\Delta\rho)^2 \Phi(1-\Phi) \tag{9}$$

It is important to note the integration limits in Equations (7) and (8). The two way path from correlation function to the scattering intensity and back requires knowledge of γ in a wide range of r and of $d\sigma/d\Omega$ in a wide range of Q. At the very least, one has to make sure that the integrands in these equations have peaked within the limits of experimental data. The correlation function for porous media for larger features can be determined via the phase function $Z(\mathbf{x})$ and Equation (6) (using statistical analysis of microscopic images, including SEM; e.g., Ioannidis et al. 1996). For SAS data, due to experimental limitations at small Q-values, increased accuracy is achieved for smaller features (i.e., larger Q-values). Therefore for rock-like materials which may have very broad distribution of microstructural feature sizes, it is useful to combine SAS and microscopy data which overlap in the intermediate size range (Radlinski et al. 2004a).

The chemical composition of rocks can vary from near uniform (e.g., pure silica for sandstones) to complex mixtures of inorganic oxides and organic matter (e.g., for oil-bearing mudstones). The validity of two phase approximation for a particular type of rock and radiation needs to be verified on a case-by-case basis by direct calculation of the scattering length density.

Special cases

Form factor for simple shapes and scattering by polydisperse system of spheres. Traditional expression of the scattering cross section follows on from Equation (7):

$$I(Q) = 4\pi(\Delta\rho)^2 \Phi(1-\Phi) F(Q) \tag{10}$$

where $F(Q) = \int_0^\infty r^2 \gamma(r)\,[\sin(Qr)/Qr]dr$ is the so-called form factor. There are analytical expressions for the form factor for simple geometrical objects like spheres, discs and parallelepipeds which can be specialized for limiting cases of 2D (flat discs) and 1D (needles) scattering objects. Feigin and Svergun (1987) and Espinat (1990) (in French) present excellent reviews of the subject.

Small-angle scattering curves for rocks often exhibit a negative power law, $I(Q) = AQ^{-m}$, where A is a constant and $3 < m < 4$. Schmidt (1982) has shown that power law scattering intensity can be explained theoretically if the scattering occurs on a particular polydisperse distribution $f(r)$ of randomly oriented independently scattering particles of any shape (provided that the particle shape distribution is independent of the distribution of particle dimensions, r):

$$f(r) \propto r^{(-2d+1-m)} \tag{11}$$

where d is the particle dimensionality. For three dimensional particles, the theoretically possible range of m is $0 < m < 4$.

This work was published shortly before the concept of fractal geometry (Mandelbrot 1977, 1982) became widely known and applied to SAS in rocks (see following section). These results were later re-formulated to accord with fractal geometry (Schmidt 1989). Recently, Radlinski et al. (2004a,b,c) have demonstrated that the polydisperse spherical pore (PDSP) model can be used to accurately describe various aspects of the micro-architecture of sedimentary rocks, beyond the limitations of fractal models.

The PDSP model assumes that the pore space of a rock can be represented by a polydisperse distribution of independently scattering spheres. The form factor for a homogeneous sphere of radius r is:

$$F_{sph}(Qr) = \left[3 \frac{\sin(Qr) - Qr\cos(Qr)}{(Qr)^3} \right]^2 \tag{12}$$

and the scattering intensity per unit volume of polydisperse spheres is given by (Guinier and Fournet 1955):

$$I(Q) = (\rho_1 - \rho_2)^2 \frac{\Phi}{\bar{V}_r} \int_{R_{\min}}^{R_{\max}} V_r^2 f(r) F_{sph}(Qr) dr \tag{13}$$

where $\bar{V}_r = \int_0^\infty V_r f(r) dr$ is the average pore volume and $f(r)$ is the probability function of the pore size distribution.

For numerical evaluation of $f(r)$, the scattering intensity can be expressed as

$$I(Q) = \sum_i IQ_{0i} \frac{\int_{R_{\min}}^{R_{\max}} V_r^2 F_{sph}(Qr) dr}{\left(R_{\max,i} - R_{\min,i}\right)} \tag{14}$$

where R_{max} and R_{min} are the maximum and minimum pore radii, respectively, and

$$IQ_{0i} = \frac{(\rho_1 - \rho_2)^2 \Phi}{\bar{V}_r} f(r_i)(R_{\max,i} - R_{\min,i}) \tag{15}$$

Equation (14) can be solved numerically for $f(r)$ using the PRINSAS software (Hinde 2004). An analytical solution for $f(r)$ has been derived by Letcher and Schmidt (1966); also see page 232 of Feigin and Svergun (1987).

Total porosity (Φ) can be determined by summing the volume of all pores and dividing by the sample volume. The specific surface area for a probe size r can be calculated from the pore size distribution by summing the surface areas of all pores of radius larger than r and dividing by the sample volume:

$$\frac{S(r)}{V} = n_v \int_r^{R_{\max}} A_r f(r') dr' \tag{16}$$

where the average number of pores per unit volume $n_v = \Phi / \bar{V}_r = I(0)/[(\rho_1 - \rho_2)^2 \bar{V}_r^2]$, $S(r)$ is the total surface area of pores with radius larger than r and $A_r = 4\pi r^2$.

Scattering by a sharp interface – Porod limit. The large-Q limit of the small-angle scattering domain is the region where atomic resolution has not been achieved, but where the observation scale is small and a well-defined interface appears to be smooth. This is the so-called Porod region (Porod 1951; Debye et al. 1957). At this limit, the differential scattering cross section for a two-phase system with a sharp interface is:

$$\frac{d\sigma}{d\Omega}(Q) = 2\pi(\rho_1 - \rho_2)^2 Q^{-4} \frac{S}{V} \tag{17}$$

where S is the total area of the interface inside the scattering volume V. If the contrast value is known, the intercept of the plot of $Q^4 I(Q)$ versus Q (the Porod plot) provides the value for the specific internal surface area, S/V.

This result is explicitly dependent on the existence of a sharp and smooth interface region, but (with subtle modifications discussed in detail by Auvray and Auroy 1991) applies to any shape of three dimensional scattering particle. Figure 3a shows the SAS curve calculated for a single sphere according to Equation (12). For large Q-values (the Porod limit) the oscillations merge into a Q^{-4}-like envelope. A small amount of polydispersity, expected in a physical system of real spheres, would average out the oscillations (as would the finite Q-resolution of

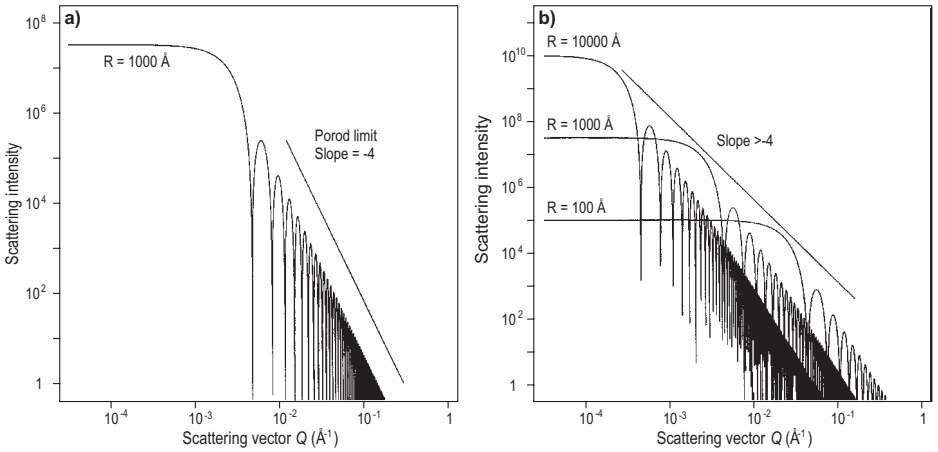

Figure 3. Results of numerical simulations of small-angle scattering for solid spheres: (a) scattering intensity for a single sphere of radius 1000 Å, (b) scattering curves for spheres of radii 10000, 1000 and 100 Å (after Radlinski et al. 2000a).

a SANS instrument). Figure 3b illustrates the effect of extensive polydispersity, similar to that theoretically discussed by Schmidt (1982). The slope of the scattering curve is now markedly larger than −4 (Radlinski et al. 2000a).

Scattering by rough surfaces: fractals and fuzzy interface. Correlation functions derived from microscopic data and power law SAXS and SANS curves obtained in the 1980's (see Background section) indicate that sedimentary rocks are fractal at microscopic scales. The early debate focused on whether rocks were mass fractals (akin to some colloidal systems) or surface fractals (as conceptually, there may be both surface and mass fractal structures present in a rock, Wong (2006)). A good discussion of small-angle scattering from fractals is presented in Schaefer et al. (1987), Martin and Hurd (1987) and Teixeira (1988).

Surface fractals are bulk objects with a rough surface—the roughness being scale invariant within a certain range of sizes. For surface fractals, the majority of the individual building blocks remain in the bulk. The surface area is proportional to r^{Ds}, where the surface fractal (Hausdorff) dimension D_s lies in the range $2 \le D_s < 3$ and r is the linear scale (the length of the measuring stick). A good example of a surface fractal is planet Earth with its rough surface morphology for which D_s varies from 2 to 2.5, depending on geographical position and length scale.

For mass (volume) fractals the majority of building blocks are exposed on the surface. The volume and consequently, the mass of a mass fractal is proportional to r^{Dm} (where the mass fractal dimension D_m can be no larger than 3). An example is a river tributary system or a network of cracks in a solid. In the latter case the relative position of matter and void is reversed and the term "pore fractal" is sometimes used.

As rocks are physical objects, fractals related to rock microstructure can only exist from near-atomic scales (the building blocks can be reasonably expected to have linear size $r_o \le 20$ Å) to an upper limit, termed a correlation length (denoted η for mass fractals and ξ for surface fractals, respectively). The correlation length is normally of the order of the grain size for a surface fractal and of the order of the largest pore diameter for a mass fractal. A specific form of the scattering law has been derived for both types of fractal objects. For mass fractals a good approximation for the correlation function for linear scales much longer than the size of the building block is (Freltoft et al. 1986):

$$\gamma(r) \propto r^{D_m-3} \exp(-r/\eta) \tag{18}$$

where the power term is the correlation function for a perfect (mathematical) mass fractal (Schaefer and Keefer 1984) and the exponential term reflects the upper-size-limit-related decay of fractal properties. For Q-values much smaller than $1/r_o$, where r_o is the size of the building block, the scattering cross section for a single mass fractal particle occupying a volume ν_0 and having average scattering length density ρ_s (Freltoft et al. 1986) is:

$$I(Q) = v_0(\rho_s - \rho_0)^2\{1 + C_0\, Q^{-1}\Gamma(D_m - 1)\eta^{Dm-1} \times \left[1 + (Q\eta)^2\right]^{\frac{1-D_m}{2}} \sin\left[(D_m - 1)\arctan(Q\eta)\right]\} \tag{19}$$

where ρ_0 is the scattering length density of embedding medium and C_0 is a constant. Furthermore, for $Q << 1/r_o$ the first term in curly brackets is insignificant in comparison to the second term—it only becomes significant in the large-Q limit of the small-angle scattering region (for full discussion see Freltoft el al. (1986)). A formulation of Equation (19) for a macroscopic sample of aerogels containing mass fractal particles of known density is given by Vacher et al. (1988). The limiting behavior of $I(Q)$ for sizes well below the correlation length, $\eta Q >> 1$, is:

$$I(Q) \propto Q^{-Dm}\Gamma(D_m - 1) \times \sin\left[(D_m - 1)(\pi/2)\right], \quad D_m \le 3 \tag{20}$$

which is the $I(Q) = const\ Q^{-Dm}$ power law expected for mathematical mass fractals.

The correlation function for real surface fractals (Bale and Schmidt 1984; Mildner and Hall 1986) has a form similar to its counterpart for mass fractals:

$$\gamma(r) = \left(1 - C(r/\xi)^{3-D_S}\right)\exp(-r/\xi) \tag{21}$$

where the first term is the correlation function for perfect surface fractals (Bale and Schmidt 1984). The exponential term describes the decay of fractal properties as the length scale approaches the upper limit ξ, $C = N_0/[4\Phi(1-\Phi)V]$, V is the scattering volume, Φ is porosity and N_0 is a constant equal to the total surface area S separating the two phases in the sample when $D_s = 2$. The Fourier transform of $\gamma(r)$ gives:

$$I(Q) = AQ^{-1}\Gamma(5 - D_S)\xi^{5-D_S}\left[1 + (Q\xi)^2\right]^{\frac{D_S-5}{2}} \sin\left[(D_S - 1)\arctan(Q\xi)\right] \tag{22}$$

where $A = \pi N_0(\Delta\rho)^2$.

Allen (1991) proposed a modified expression for the correlation function for surface fractals (Eqn. 21) based on the assumption that the fractal surface is self-affine and that the surface area per unit volume, $(S/V)_r$, scales with the roughness scale, r, as follows:

$$(S/V)_r = (S/V)_0(r/\xi)^{2-D_S} \tag{23}$$

Equation (23) relates the specific surface area at any length scale, $(S/V)_r$, to its "smooth" value, $(S/V)_0$, measured with the roughness length scale ξ (where the correlation length ξ represents the upper limit for surface fractal properties). In this notation the constant A in Equation (22) is $A = \pi\xi^{Ds-2}(S/V)_0(\Delta\rho)^2$. For $D_s = 2$, $(S/V)_0 = N_0$, as expected.

The limiting behavior for sizes well below the correlation length, $\xi Q >> 1$, is given by the expression derived by Bale and Schmidt (1984) for unconstrained surface fractals:

$$I(Q) = A\, Q^{D_s-6}\Gamma(5 - D_s) \times \sin\left[(D_s - 1)(\pi/2)\right], \quad 2 < D_s \le 3 \tag{24}$$

where $A = \pi N_0(\Delta\rho)^2$. This is an $I(Q) = const\ Q^{Ds-6}$ power law which reduces to the Porod limit for $D_s = 2$.

The specific form of the small-angle scattering law, $I(Q) = constant \times Q^{-m}$, has been derived by many authors for both ideal and real surface fractals as well as mass fractals. It is important to note that transitional effects near the upper and lower limit of the fractal region may distort the scattering curve over a significant Q-range (Freltoft et al. 1986; Allen 1991). It is usually assumed that in order to justify the notion of a fractal, the appropriate geometrical properties should extend over at least one order of magnitude of the length scale (see discussion in Radlinski et al. 1996a).

Exponent m is D_m for mass fractals and 6-D_s for surface fractals. Since the allowed values for fractal dimensions are restricted ($2 < D_s \leq 3$ for surface fractals and $D_m \leq 3$ for mass fractals), the power law exponent is $m < 3$ for mass fractals and $3 < m \leq 4$ for surface fractals, where $m = 4$ for smooth surfaces (Porod law). This allows for a clear distinction between the two types of fractals using SAS techniques.

There is another class of scattering curve, for which the power law exponent is less than the Porod limit value of –4. Such a situation arises when a non-fractal porous medium has a fuzzy interface, i.e., characterized by a value of the scattering length density monotonously varying over a distance corresponding to the interface thickness. This can be achieved by coating the surface with a thin molecular layer. For fuzzy interfaces the scattering law has been theoretically predicted to have the form $I(Q) = const\ Q^{-m}$, where $4 < m < 5$ (Schmidt et al. 1991; McMahon et al. 2001).

The extended regions of power-law scattering curves (where the exponent $m = 1$ or $m = 2$), are observed for scattering on (non-fractal) one-dimensional particles (needles) or two-dimensional particles (platelets), respectively (Feigin and Svergun 1987; Espinat 1990). Radlinski et al. (1996b) show an example of SANS and SAXS scattering on a molecular system undergoing a thermally-driven 1D ($m = 1$) → 2D ($m = 2$) → 3D ($m = 4$) transition.

CALCULATIONS OF THE SCATTERING LENGTH DENSITY AND CONTRAST

General expressions

A knowledge of contrast is crucial for quantitative interpretation of absolutely calibrated SANS (and SAXS) results. In geological applications, a value for contrast is needed to determine rock porosity, internal specific surface area and other related quantities. Analysis of contrast values constitutes an integral part of preparations for a SAS experiment and often determines which instruments need to be used in order to best address the problem at hand. For this reason we provide a comprehensive discussion of the subject, including three worked examples of contrast calculation.

Rocks are somewhat transparent to neutrons and to a much lesser extent, X-rays. Therefore, these two particular types of radiation can be used for scattering experiments on geological samples. The physical property responsible for neutron scattering is the coherent scattering amplitude (nuclear potential)—for X-rays it is the electron density (electric charge). The strength of radiation-matter interaction that influences the contrast term, $(\Delta\rho)^2$, in Equation (7), is dependent on the average of all the nuclei in a pseudo-molecule whose chemical composition reflects the average composition of each of the two rock phases: the solid phase (rock matrix) and the fluid phase (the content of the pore space). The neutron scattering length density for each single phase of pseudo-molar mass M is:

$$\rho_n = \frac{N_A d}{M} \sum_j p_j \left(\sum_i s_i b_i \right)_j \tag{25}$$

where $N_A = 6.022 \times 10^{23}$ is the Avogadro's number, d is density (in g/cm^3), s_i is the proportion

by number of nucleus i in the compound j, p_j is the proportion by molecular number of the compound j in the mixture and b_i is the coherent scattering amplitude for nucleus i.

For X-ray coherent (also called Rayleigh or elastic) scattering, the single-phase factor in the contrast term is simply:

$$\rho_{el} = I_e \rho_e = \frac{N_A d}{M} N_e I_e \tag{26}$$

where ρ_e is the electron density (i.e., number of electrons per unit volume), $I_e = e^2/(mc^2) = 2.82 \times 10^{-13}$ cm is the coherent scattering amplitude of a single electron, N_e is the number of electrons per one supra-molecule (of composition as per the double summation in Eqn. 25), M is the molecular weight of one supra-molecule and d is bulk density (in g/cm^3).

Scattering length density for common rock constituents

General data. Table 1 lists the coherent scattering amplitude, b (Sears 1990; Dianoux and Lander 2002), atomic mass (in atomic units) and the number of electrons, Z, for 15 elements, including those commonly found in inorganic and organic rocks. Density and molar weights for most common naturally abundant inorganic minerals are compiled in Table 2. Table 3 lists the neutron and X-ray scattering length densities for these minerals.

Compositional data obtained by X-ray fluorescence for two types of inorganic matter—Palaeozoic shale (Radlinski et al. 1996a) and ash from a Bowen Basin Permian coal (Radlinski et al. 2004c)—are presented in Table 4. Calculated crystalline density for these two rocks is 2.98 g/cm^3 for shale and 3.23 g/cm^3 for ash, whereas the measured density of the shale sample is 2.4 g/cm^3, i.e., 81% of the crystalline value. This 19% difference cannot be accounted for by sample porosity, as the porosity is only 5%. It is likely that at least some of the oxides comprising the rock are in an amorphous state (and are less densely packed than the crystalline state). The scattering length density (SLD) calculated from Equation (25) is 4.47×10^{10} cm^{-2} for shale (crystalline) and 4.79×10^{10} cm^{-2} for ash (crystalline). Taking into account the ~20% decrease in density for naturally abundant inorganic matter, these values are likely to be about 3.6×10^{10} cm^{-2} for shale and 3.75×10^{10} cm^{-2} for ash.

Table 1. Average coherent scattering amplitude of neutron scattering for naturally abundant isotopes, atomic mass and number of electrons for 15 elements commonly found in inorganic and organic rocks.

Element	b (10^{-12} cm)	Atomic mass (au)	Atomic No.
H	−0.3739	1.00794	1
D	0.6671	2.0	1
C	0.6646	12.011	6
N	0.936	14.007	7
O	0.5803	15.9994	8
Mg	0.5375	24.3050	12
Al	0.3449	26.982	13
Si	0.4149	28.0855	14
P	0.513	30.974	15
S	0.2847	32.066	16
K	0.371	39.0983	19
Ca	0.490	40.078	20
Ti	−0.330	47.867	22
Fe	0.954	55.845	26
Zr	0.716	91.224	40

Table 2. Density and molar weight for common naturally abundant inorganic minerals, water and heavy water. Abbreviations used: cr – crystalline, am – amorphous.

Mineral	Formula	Density (g/cm^3)	Molecular Wt. (g/mole)
Quartz	SiO_2	2.7; 2.2 (fused)	60.085
Corundum	Al_2O_3	4.0	101.96
Hematite	Fe_2O_3	5.2	159.69
Anatase	TiO_2	3.9	79.865
Periclase	MgO	3.6	40.304
Lime	CaO	3.25-3.38	56.077
	K_2O	2.32	94.196
Zircon	$ZrSiO_4$	4.72 cr, 4.0 am	183.3071
Water	H_2O	1.0	17.999
Heavy water	D_2O	1.105	19.999

Table 3. Neutron, ρ_n, and X-ray, ρ_{el}, scattering length densities (SLD) for common minerals, water and heavy water. The value of $\Sigma s_i b_i$ (Eqn. 9) is shown in the last column.

Mineral	Formula	SAXS SLD ρ_{el} (10^{11} cm^{-2})	SANS SLD ρ_n (10^{10} cm^{-2})	$\Sigma s_i b_i$ (10^{-12} cm)
Quartz	SiO_2	2.29	4.264	1.5755
Corundum	Al_2O_3	3.332	5.743	2.4307
Hematite	Fe_2O_3	4.205	7.156	3.6489
Anatase	TiO_2	3.152	2.443	0.8306
Periclase	MgO	3.034	6.014	1.1178
Lime	CaO	2.816	3.817	1.0703
	K_2O	1.924	1.962	1.3223
Zircon	$ZrSiO_4$	2.702	—	—
Water	H_2O	0.94	–0.56	–0.1675
Heavy water	D_2O	0.94	6.4	1.9145

Table 4. Comparison of chemical composition for coal ash and typical shale (in wt% units).

Mineral	SiO_2	Al_2O_3	Fe_2O_3	TiO_2	CaO	K_2O	MgO	balance	total
Ash	49	25	13	1.3	1.0	1.0	—	9.7	100
Shale	58	13.4	6.7	-	3.1	3.1	2.4	13.3	100

SLD for neutrons. The values of ρ_n (for neutrons) are presented graphically in Figure 4. On the left hand side, open arrows indicate SLD values for individual inorganic minerals calculated using crystalline densities (Tables 2 and 3). Heavy arrows indicate SLDs of particular interest: for (partly) amorphous shale and ash, void, and light and heavy water. For sedimentary rocks void represents pore space (which is typically filled with water). Therefore, the typical contrast value is given by the square of the difference between the SLD for the shale and the SLD for the water.

Due to the large coherent scattering amplitude associated with deuterium (Table 1), the scattering length density for heavy water is very large. For instance, by saturating a rock sample with a mixture of water and heavy water of appropriate proportions one can match the scattering length density of the rock matrix and remove the matrix-void scattering contrast. Contrast matching (as well as contrast enhancement) by spatially selective deuteration is

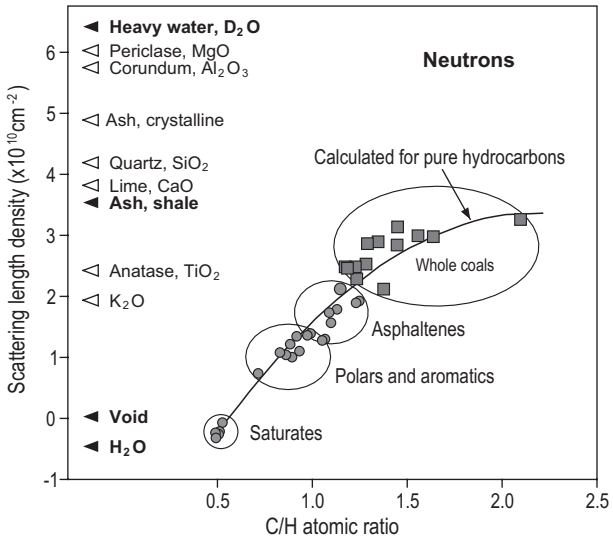

Figure 4. Neutron scattering length density for coals, hydrocarbons and common minerals.

arguably the most important feature unique to neutron scattering and has been widely employed in numerous studies. The most celebrated applications of contrast matching are in polymer science and biology. In the context of rock microstructure, contrast matching has been recently used by Broseta et al. (2001) to study capillary condensation of water in the pores of sandstone and by Snook et al. (2002), using d-toluene to determine closed porosity in coal chars used as fuel in industrial blast furnaces.

On the right hand side of Figure 4 we show values of SLD for organic compounds: whole coals (comprised of various solid organic macerals), fractions of crude oil (asphaltenes, polars and aromatics, and saturates) and pure hydrocarbons. For organic compounds, the value of SLD is largely determined by the atomic ratio of two dominant elements in the organic matter—carbon and hydrogen. As there is little neutron contrast between the solid organic and solid inorganic components of the rock, for rocks containing both organic and inorganic solid matter (e.g., hydrocarbon source rocks, ashy coals) the dominant scattering contrast is between the solid matrix and the pore space. Importantly, therefore, neutrons perceive sedimentary rocks as two-phase scattering systems, independent of the organic matter content.

At depths and temperatures corresponding to the oil generation window, for hydrocarbon source rocks the solid organic matter will gradually decompose into viscous bitumen, crude oil and eventually crack to light hydrocarbons and gas. This is accompanied by an increase in volume, leading to displacement of formation water with liquid hydrocarbons - a process known as primary migration. Due to the changes in pore fluid composition that take place during primary migration, hydrocarbon generation and expulsion in source rocks can be observed using SANS (Fig. 4).

SLD for X-rays. Values of scattering length density for X-rays, ρ_{el}, are plotted in Figure 5. It is apparent that ρ_{el} is strongly correlated with the density of the scattering material. Importantly, the matrix-void scattering contrast for organic matrix is about 25% of that of inorganic matrix. If the rock is purely organic (e.g., ash-free coal) or purely inorganic (e.g., sandstone), the system remains two-phase and the structural information obtained from both SAXS and SANS is identical. For rocks with both a significant organic and inorganic component, however, the

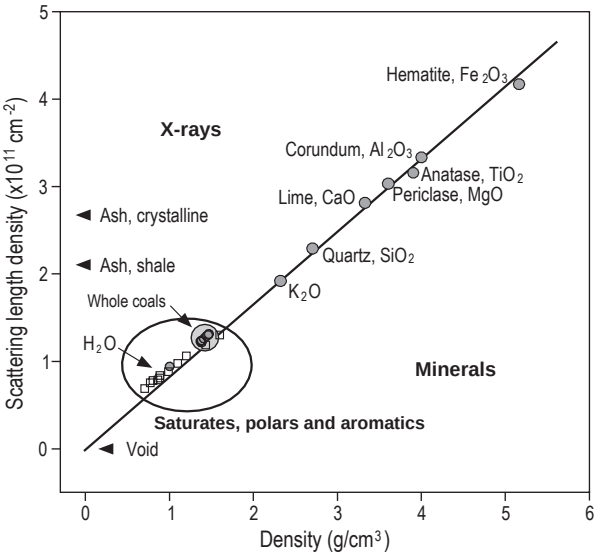

Figure 5. X-ray scattering length density for coals, hydrocarbons and common minerals.

system is two-phase for SANS, three-phase for SAXS and the scattering data obtained with the two techniques are no longer equivalent (Radlinski et al. 1996a).

Scattering lengths shown in Figure 5 have been calculated for X-ray photon energy of the incident primary beam which is greater than the excitation energy of inner electronic shells. When the absorption edge of an atom is close to the X-ray photon energy, the dispersion corrections to the coherent scattering amplitude can be up to 50% of the value given by Equation (26). With synchrotron X-ray sources it is possible to tune X-ray energy to the absorption edge of selected atoms, which results in enhanced contrast variation.

Selected examples

SANS - scattering length density for corundum. Corundum is one of the most abundant minerals in the Earth's crust. For Al_2O_3, Equation (25) reduces to one term only (there is no summation over j) and index i assumes values from 1 (for Al) to 4 (2, 3 and 4 for the three naturally abundant isotopes of oxygen). Coherent scattering amplitudes for naturally abundant isotopes are well known (Sears 1990, Dianoux and Lander 2002). Aluminium has one stable isotope, ^{27}Al ($s_1 = 2$, $b_1 = 0.3449 \times 10^{-12}$ cm) and oxygen has three: ^{16}O (natural abundance 99.76%, atomic mass 15.99491), ^{17}O (natural abundance 0.04%) and ^{18}O (natural abundance 0.20%). The three oxygen isotopes exhibit three coherent scattering amplitudes (b): $b_2 = b(^{16}\text{O}) = 0.5803 \times 10^{-12}$ cm, $b_3 = b(^{17}\text{O}) = 0.578 \times 10^{-12}$ cm and $b_4 = b(^{18}\text{O}) = 0.584 \times 10^{-12}$ cm. For a mineral with a naturally occurring isotopic distribution, the three values of b_i ($i = 1, 2, 3$) can be substituted with the abundance-weighted average value of $b_{ave} = 0.5803 \times 10^{-12}$ cm. An average atomic mass of 15.9994 can now be used (Table 1), and the range of index i in Equation (25) is reduced to (1, 2). Substituting $b_2 = b_{ave}$, $s_2 = 3$, and using a density of 4.0 g/cm^3 and a molar mass of 101.96 g (Table 2), one can calculate from Equation (9) the scattering length density for crystalline corundum: $\rho_n = 5.743 \times 10^{10}$ cm^{-2}.

SANS - Scattering length density for coal. Typical results of chemical (ultimate) analysis of a coal are shown in Table 5: the amount of ash and elements H, C, N, S and O are all expressed in weight %. Two sets of numbers are given for each element - one is a percentage of dry mass with ash (dry), and the other is dry ash free (daf).

Table 5. Typical results of chemical analysis of a coal (Ammonate whole coal, vitrinite reflectance Ro = 1.28%). All numbers are in wt%.

Ash dry	H dry	H daf	C dry	C daf	N dry	N daf	S dry	S daf	O dry	O daf
11.63	4.63	5.24	79.4	89.849	1.35	1.53	0.64	0.72	2.35	2.659

Table 6. Atomic proportion (s_i of Eqn. 25) for five elements in a pseudo-molecule of dry ash free Ammonate whole coal. Note that daf weight percents add up to 100%.

Element	H	C	N	S	O
wt%	5.24	89.849	1.53	0.72	2.659
s	5.198	7.481	0.109	0.0225	0.166

To calculate ρ_n from Equation (25), assume the organic matrix of coal is composed of identical pseudo-molecules of composition $H_tC_uN_vS_xO_y$, where the generally non-integer numbers t, u, v, x, and y are the atomic proportions (i.e., numbers of atoms in a pseudo-molecule, s_i of Eqn. 25) for hydrogen, carbon, nitrogen, sulfur and oxygen, respectively. The atomic proportion for each chemical element is defined as the ratio of its dry ash free weight percent to its atomic mass. Table 6 lists atomic proportions calculated using data from Tables 5 and 1.

Because of the way atomic proportions are defined, the molar weight (M) of the molecule $H_tC_uN_vS_xO_y$ is 100 g ($M = \Sigma_i$ (atomic proportion)$_i \times$ (atomic mass)$_i$). The scattering length density, ρ_n, can now be calculated from Equation (25) by substituting $N_A = 6.022 \times 10^{23}$, d = 1.47 g/cm^3 (obtained from direct measurement on a coal sample), M = 100 g and the s_ib_i value obtained for every element using data from Tables 1 and 6. The result is $\rho_n = 2.86\text{x}10^{10}$ cm^{-2}.

SAXS - scattering length density for zircon. Zircons are sub-millimeter size crystals used for U-Pb dating of geological systems. Zircon crystals are too small for SANS measurements with currently available instruments (generally less than 1 mm across), but the geometry and volumetric fraction of radiation damaged (metamict) regions in zircons can be determined using SAXS utilizing the amorphous-crystalline contrast (Radlinski et al. 2003).

Consider a zircon crystal of composition $ZrSiO_4$. Both Zr (atomic mass 91.224, 40 electrons) and Si (atomic mass 28.0855, 14 electrons) have only one naturally abundant stable isotope. For the three oxygen isotopes, the average value of atomic mass is 15.9994 and the number of electrons per atom is 8 (Table 1). Therefore, the molar mass of $ZrSiO_4$ is 91.224 + 28.0855 + 4 × 15.9994 = 183.3071 grams, and the total number of electrons in one molecule is 40 + 14 + 4 × 8 = 86. The scattering length density, ρ_{el}, for crystalline zircon can now be calculated from Equation (26) by substituting $I_e = e^2/(mc^2) = 2.82 \times 10^{-13}$ cm, $N_A = 6.022 \times 10^{23}$, M = 183.3071 g, N_e = 86 and the crystalline density d = 4.27 g/cm^3 (Table 2). The result is $\rho_{el} = 3.757 \times 10^{11}$ cm^{-2}. For amorphous (metamict) zircon the only difference is the density, which now is d = 4.0 g/cm^3 (Table 2). The resulting scattering length density is $\rho_{el} = 3.184 \times 10^{11}$ cm^{-2}.

HOW A SANS EXPERIMENT IS UNDERTAKEN

Measurement of the absolute scattering cross section

For a pinhole SAS instrument (schematic diagram shown in Fig. 1), the signal registered by each element (pixel) of a two dimensional detector (whose position is defined by the scattering vector **Q** and the solid angle element $d\Omega$), is the number of counts $I(\mathbf{Q})$. $I(\mathbf{Q})$ is

proportional to the number of neutrons (or X-ray photons) scattered by the illuminated volume of a sample of surface area A and thickness t:

$$I(\mathbf{Q},d\Omega) = I_0 AtT \frac{d\sigma}{d\Omega} d\Omega E(\mathbf{Q},\lambda) + \text{background} \quad (27)$$

where λ is the wavelength, T is sample transmission, I_0 is the incident beam intensity and $E(\mathbf{Q}, \lambda)$ is the quantum efficiency of the detector element. The background term reflects electronic noise associated with the electronic detection system and external radiation (including high-energy cosmic radiation).

The purpose of an SAS experiment is to determine (for a number of samples) the value of the differential scattering cross section, $d\sigma/d\Omega$, in absolute units of cm^{-1}. In laboratory practice this is often done in the following sequence:

1. Measure the thickness and transmission for all samples
2. Run a standard sample of known t, T and $d\sigma/d\Omega$ in absolute units
3. Measure the dark current, i.e., background signal, with a platelet of cadmium for SANS (or lead for SAXS) placed in the sample position
4. If a sample is placed in a cell, measure the scattering from the empty cell
5. Measure the scattering from a series of samples using the same slits used for the standard sample
6. At the end of experiment re-run the dark current measurement

Absolutely calibrated data enable quantitative comparison with theoretical models. Leading SAS laboratories develop and calibrate scattering standards, including inter-laboratory calibration and SANS-SAXS cross-calibration (e.g., Ibel and Wright 1980, Wignall and Bates 1987, Russell et al. 1988). For an SAS experiment conducted in the manner described above, the scattering data (i.e., $I(\mathbf{Q},d\Omega)$) for a standard sample are used to determine the value of $Ad\Omega E(\mathbf{Q},\lambda)$ from Equation 27 (since I_0 is continuously monitored and the background scattering is measured independently). The result is then used to calculate $d\sigma/d\Omega$ in absolute units for every measured sample.

By following the above procedure it is also possible to process data from the first sample before running subsequent samples. Furthermore, useful results can be obtained even if SAS data for some of the samples were not acquired or were corrupted. A series of SANS experiments may take several days to complete, and there is always a possibility of unexpected reactor shut down (which is the most common cause of incomplete data acquisition).

Measurement of transmission

Transmission (T) is measured in a separate experiment by measuring the total intensity of radiation with (I^{tot}), and without (I_0^{tot}) a sample in the beam ($T = I^{tot} / I_0^{tot}$). One method used to measure transmission is to insert a total neutron counter a short distance downstream from the sample position to measure the signal with and without the sample in the beam. Leading SANS and SAXS laboratories have well tested procedures for transmission measurements.

Sample thickness

In the case of a liquid contained in a cell or a self-supporting solid, the measurement of sample thickness is trivial. Geological samples, however (especially those originating from exploration wells), are seldom available as an oriented core. The most common type of rock sample available from exploration drilling is “drill cuttings,” which need to be crushed to coarse powders for neutron scattering experiments. The grain size of the crushed sample must represent a balance between average orientation over the sample volume (the grains cannot be

too large) and the need to minimize the internal surface area associated with grain surfaces (the grains cannot be too small). Furthermore, for absolute calculations of rock properties one needs to take account of inter-granular porosity. Radlinski et al. (2004b) used resin-fixed powders of a narrow grain size distribution (0.355 – 0.475 mm) to fill the inter-granular porosity. The volume associated with the inter-granular porosity can then be determined both by calculation and by comparison with scattering data for solid samples. Spalla et al. (2003) used saturation with solvents to eliminate the need for thickness measurements in SAXS work on powders deposited onto a Kapton sheet. For powdered samples, to avoid significant contribution from scattering from the surface of individual grains, the grain size should be at least 10 times larger than the maximum linear distance accessible with the scattering apparatus (~$1/Q_{min}$). Ideally, the minimum acceptable grain size should be determined experimentally.

MICROSTRUCTURE OF ROCKS REVEALED BY SANS - EXAMPLES

Sandstones

Scale range of fractal and Euclidean microstructure. Sandstones are composed predominantly of quartz with small amounts of interstitial clay and/or mica minerals. Subsurface sandstones constitute reservoir rocks for both water and hydrocarbons and have been extensively studied—especially in engineering applications related to porosity, permeability and fluid flow. As discussed previously, in the 1980's sandstone microstructure has been recognized to have a non-universal surface fractal character. The range over which the fractal behavior in sandstones has been observed by SAS was extended to about 20 μm using a then newly constructed low-background USANS instrument (Agamalian et al. 1997; Radlinski et al. 2000b). The observation limit was further extended to about 0.5 mm by combining SANS, USANS and backscattering scanning electron microscopy (BSEM) data (Radlinski et al. 2004a).

Figure 6 shows the absolute scattering intensity for a sample of sandstone presented on a log-log scale. Over 4.5 orders of magnitude on the length scale (from $2.5/Q$ = 1 nm to 50 μm), the pore-matrix interface is a surface fractal (D_s = 2.47). Over the corresponding Q-range, the scattering intensity varies over 17 orders of magnitude (from 10^{-3} cm^{-1} to 10^{14} cm^{-1}). Note

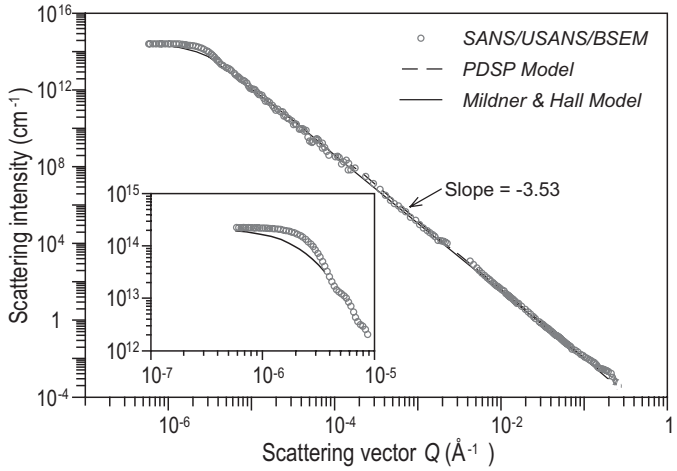

Figure 6. Absolutely calibrated SANS scattering intensity for a coarse sandstone, after background subtraction of 6×10^{-3} cm^{-1} (after Radlinski et al. 2004a).

that intensity values over 10^{11} cm^{-1} are inferred from the Fourier transform of the Backscatter Electron Microscopy (BSEM)-determined correlation function (Eqn. 5). For pore sizes larger than $2.5/Q$ = 50 μm, the scattering curve flattens out, indicating a transition to a Euclidean scattering regime.

This particular rock is composed of 98% quartz, 1.5% mica and small amounts of dickite and montmorillonite (Radlinski et al. 2004a). The average grain diameter is approximately 250 μm and the porosity is 0.181. The value of porosity calculated from the invariant (Eqn. 9) agrees with an independently measured value to within 5%. The correlation length (ξ) (obtained by a reasonably good fit to the Mildner and Hall model; Eqn. 22) is 35 μm. The fit to the PDSP (polydisperse spheres) model, Equation (14), (which uses a form factor for homogeneous spheres, (Eqn. 12) and, therefore, is not constrained by an analytical form for the long-range cut-off of the correlation function) is very good. The model provides values for the specific surface area and pore size distribution (see Fig. 7), and gives an upper limit for surface fractal behavior of about 55 μm. Using this model, the volumetric fraction of total porosity associated with surface fractal geometry (Φ_{frac}/Φ_{total}) is approximately 62%.

These results demonstrate that fractal-like surface roughness can extend for a distance of approximately one fifth of the grain size diameter into the pore space, entirely controlling the specific surface area associated with molecular probe sizes and constitutes the majority of the pore volume. Only the largest pores (over 35 to 55 μm in diameter) are described by Euclidean geometry. NMR measurements of the decay of nuclear transverse magnetization in water-saturated samples indicate the existence of two scattering regimes - fractal and Euclidean (Radlinski et al. 2004a). These yield values of ξ of 35 μm and Φ_{frac}/Φ_{total} = 47% (which are in good agreement with neutron scattering data).

Synthetic mercury intrusion porosimetry curve. From the pore size distribution (see Fig. 7) and the known relationship between the capillary pressure and the pore size, it is possible to construct a synthetic mercury intrusion porosimetry (MIP) curve and compare it with the measured MIP curve. Figure 8 shows such a comparison and indicates that for this particular sample of sandstone, the ratio of the pore body size (measured by neutron scattering) to the pore throat size (measured by MIP) is about 3.5 and is independent of the pore size (Radlinski et al. 2004a).

Wetting mechanism for fractal pores. Broseta et al. (2001) published the first SAS study of the mechanism of wetting for the fractal pore-matrix interface in a rock (a Vosges sandstone with a porosity of 17%). The authors took advantage of the universal applicability of two-phase approximation for (organic matter free) sandstones: SANS and USAXS data were combined to calculate $d\sigma/d\Omega$ for dry rock samples and their fractal dimension (D_s = 2.68) was determined over three decades of the length scale. In order to observe size-specific invasion of pores by water, samples were exposed to a contrast-matched mixture of water and heavy water at several controlled vapor pressures. As the smallest pores imbibe water first, a shift of the large-Q cut-off of the fractal scattering regime towards smaller Q-values was observed with increased water vapor pressure. This was followed by Q^{-4} Porod scattering (from the smooth interface of water-filled small pores) at large Q-values. Wetting behavior was dominated by the capillary wetting regime (smallest pores filled with water first), with limited influence from the substrate-controlled wetting regime (covering a surface with a thin film of a uniform thickness) at higher water vapor pressures. The work of Broseta et al. (2001) constitutes the first direct visualization (in the Fourier reciprocal space) of the dynamics of fluid imbibition within a system of fractal pores.

In summary, SANS can be a useful technique in the analysis of fluid behavior in confined geometries (e.g., Lin et al. 1994a,b; Melnichenko et al. 2005). This application is further discussed by Cole et al. (2006, this volume).

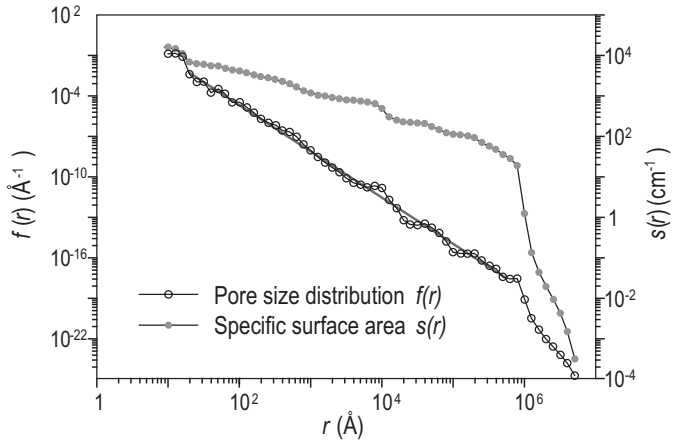

Figure 7. Distribution of pore size ($f(r)$) and specific surface area ($s(r)$) for a coarse sandstone. Straight line corresponds to $f(r) = const \times r^{-(D+1)}$ with $D = 2.49 \pm 0.03$ (after Radlinski et al. 2004a).

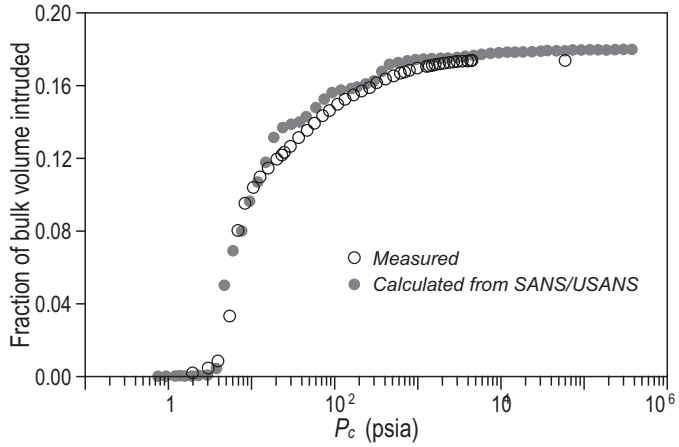

Figure 8. Measured and calculated mercury intrusion porosimetry curve for a coarse sandstone (after Radlinski et al. 2004a).

Mudstones: hydrocarbon source rocks

Principle of observation of hydrocarbon generation. Hydrocarbons are generated in organic-rich clastic rocks (e.g., mudstones) at elevated temperatures over geologic time. At the onset of bitumen generation, the organic matter expands and migrates through the pore space of the rock. This process can be detected by SANS/USANS due to the difference in contrast between the generated hydrocarbons and the pore water (Fig. 4) and has been studied for both natural (Radlinski et al. 1996a) and artificial (Radlinski et al. 2000a) hydrocarbon source rocks.

Figure 9 shows a schematic variation of SANS/USANS intensity with depth for three selected pore sizes r (corresponding to $Q \approx 2.5/r$). Two scenarios are considered – one for an organic-rich rock (in which the pore space eventually becomes saturated with generated

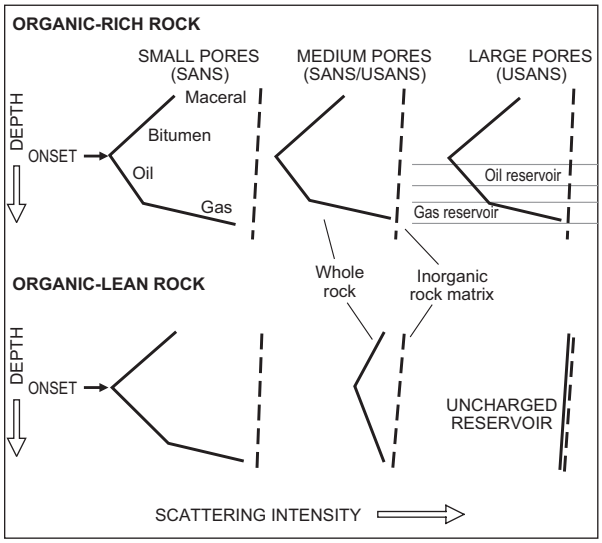

Figure 9. A schematic representation of the variation of SANS/USANS intensity with depth (at three fixed *Q*-values) for an organic-rich effective source rock (top) and an organic-lean rock (bottom) (after Radlinski et al. 2004b).

hydrocarbons and hydrocarbon expulsion ensues) and another for an organic-lean rock (for which only a fraction of the pore space is invaded by generated hydrocarbons). It is assumed that the organic matter is finely dispersed throughout the rock volume. In geochemical terms, an organic-rich rock is characterized by a TOC values greater than 2% and an organic-lean rock by a TOC values of less than 2% (where TOC is the weight percent of total organic carbon present in the rock).

Both subsurface temperature and pressure increase with depth. Under increasing pressure, the pores are expected to gradually compact. For an inorganic rock matrix (or organic-matter-free rock) of fixed lithology, the scattering intensity at a fixed *Q*-value decreases slightly with depth (as indicated by the broken lines). For rocks containing organic matter, increasing subsidence and thermal maturation results in the invasion of pore space with hydrocarbons generated from the organic source material—initially with bitumen, which then progressively cracks into lighter hydrocarbons (and eventually into gas). Using the corresponding scattering length density values for these various hydrocarbons (Fig. 4) one can schematically represent the scattering intensity versus depth as shown in Figure 9 with solid lines. Note that the scattering intensity for an organic-matter-free rock is always greater than for a rock of the same lithology containing dispersed organic matter.

The onset of oil generation occurs at a depth where maximum bitumen saturation (minimum scattering intensity) is observed for small pores. The onset of oil expulsion occurs at a depth where maximum bitumen saturation is observed for the largest pores (about 20 μm for typical shales; Radlinski et al. 1999). Only organic-rich rocks are capable of generating sufficient volumes of hydrocarbons to both fully saturate the pore space and to allow hydrocarbon expulsion from the source rock—thus becoming effective sources for hydrocarbon accumulations.

A basin-wide study of hydrocarbon generation and expulsion. These ideas were used to perform a comprehensive analysis of SANS and USANS data obtained for 165 potential source rocks of Late Jurassic - Early Cretaceous age, recovered from nine exploration wells

drilled in the Browse Basin, offshore Western Australia (Radlinski et al. 2004b). This study demonstrated that conclusions drawn from SANS and USANS data are consistent with results obtained using traditional geochemical methods and can be used to independently calibrate and refine source rock generation/expulsion scenarios derived from geochemical modeling.

Scattering patterns form the Browse Basin rock samples are fractal-like, and the PDSP model (Eqn. 14) was used for numerical analysis. Figure 10 shows an example of the results: the variation of pore number density with depth (compaction) for four selected pore sizes, calculated for the giant Brewster gas accumulation. Figure 11 illustrates a comparison of USANS results with the predictions for oil and gas generation based on traditional geochemical thermal maturity indicators and thermal history analysis of the Brewster-1A well.

Coal

Coals as source rocks for hydrocarbons. Coals (in a form of fine powders and carbon blacks) were among the first substances for which classical SAS patterns were observed (Krishnamurti 1930; Warren 1934). Coal also provided one of the first examples of a surface fractal microstructure (Bale and Schmidt 1984) and has been studied extensively by SAXS and SANS—often in relation to industrial processes (Lin et al. 1978; Winans and Thiyagarajan 1988; Johnston et al. 1993; Snook et al. 2002; McMahon et al. 2002; Prinz et al. 2004; Radlinski et al. 2004c).

In the following we provide examples of SANS and USANS results pertaining to natural (untreated) coal. Despite its origin from higher plant debris (thermally altered in anoxic conditions) and the atomic composition being dominated by carbon and hydrogen, the microstructure of the coal—pore space interface is surprisingly similar to that of inorganic sedimentary rocks (Radlinski and Hinde 2002). The coal matrix is sensitive to thermal treatment, however, and in natural conditions exhibits two types of thermally induced coal-specific phenomena:

1. At small scales, the internal specific surface area gradually decreases with increasing rank and a microstructure comprising stacked lamellae of polyaromatic hydrocarbon sheets spaced at an average repeat distance of about 25 Å is formed (while retaining a surface fractal structure at larger scales).
2. In the narrow temperature range corresponding to the onset of hydrocarbon generation, the pore space microstructure is subject to a marked rearrangement.

These two points are illustrated in Figure 12, which shows the scattering intensity versus depth (for pore size $2.5/Q = 25$ nm) and the pore number density versus depth (calculated using the PDSP model) for a series of coal samples (which have undergone increasing thermal maturation with depth) derived from a petroleum exploration well. A discussion of the formation of the lamellar structure and the evidence that it can become intercalated with clay minerals (based on comparison of SAXS and SANS data) is given in Radlinski et al. (2004c).

Adsorption of gases. The magnitude of the internal specific surface area (SSA) in a coal determines the amount of gas (like CH_4 and CO_2) that can be adsorbed as a surface monolayer. Figure 13 shows a compilation of SSA data obtained for coals and vitrinite macerals (for both solid samples oriented in-bedding-plane and standard pellets) of different rank using the N_2 adsorption method and SANS (Radlinski et al. 2004c). As neutrons can detect both effective (open) and non-effective (closed) porosity, and the presence of connate (remnant) water slightly increases the scattering contrast and decreases the number of sites available for gas adsorption, the SANS-determined SSA values are systematically higher than those derived from the N_2 adsorption method. Both methods, however, give remarkably similar trends with respect of rank (expressed as vitrinite reflectance).

Total porosity. The total porosity of coal versus rank (expressed as % of carbon in dry ash free coal sample) is presented in Figure 14 against the backdrop of the world trend determined

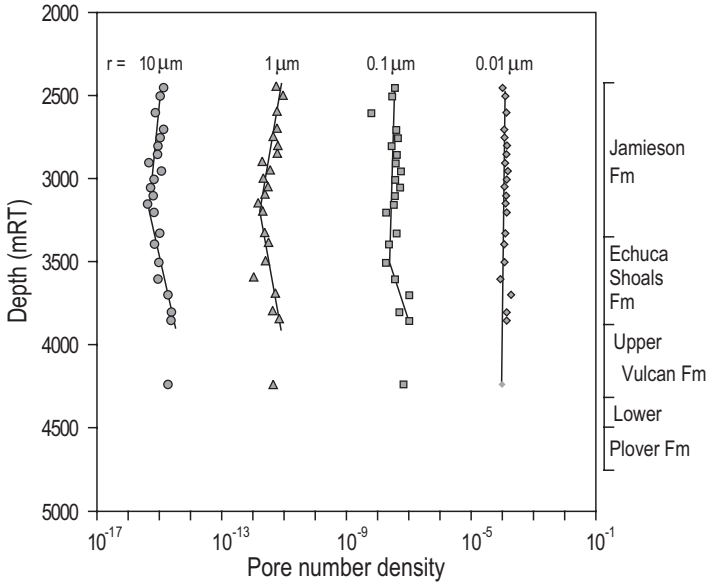

Figure 10. Variation of the pore number density for four selected pore sizes versus depth. Potential hydrocarbon source rock samples were recovered from the Brewster-1A well drilled on the giant Brewster gas accumulation, Browse Basin, Australia (after Radlinski et al. 2004b).

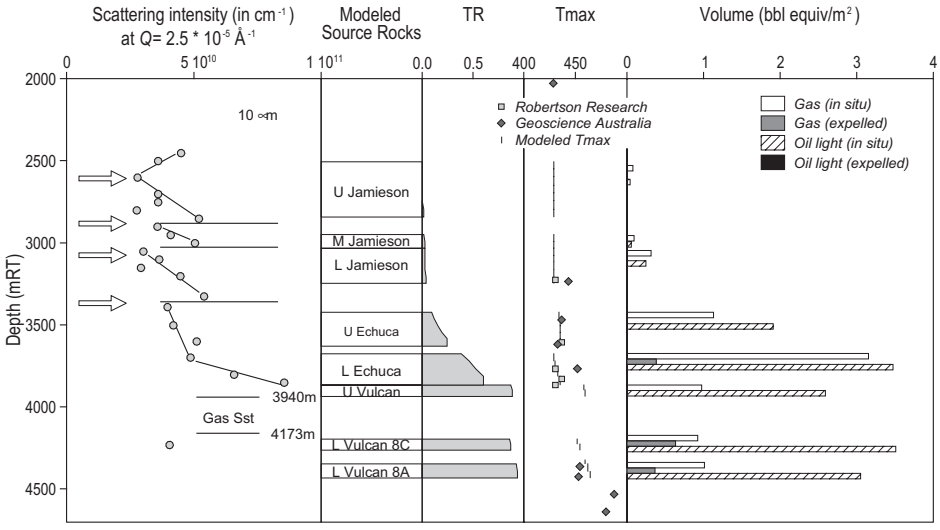

Figure 11. Comparison of USANS scattering intensity trends with modeled kerogen transformation (TR – Transformation Ratio) and *in situ* gas/oil generation and expulsion derived from geochemistry and thermal history analysis for Brewster-1A (after Radlinski et al. 2004b).

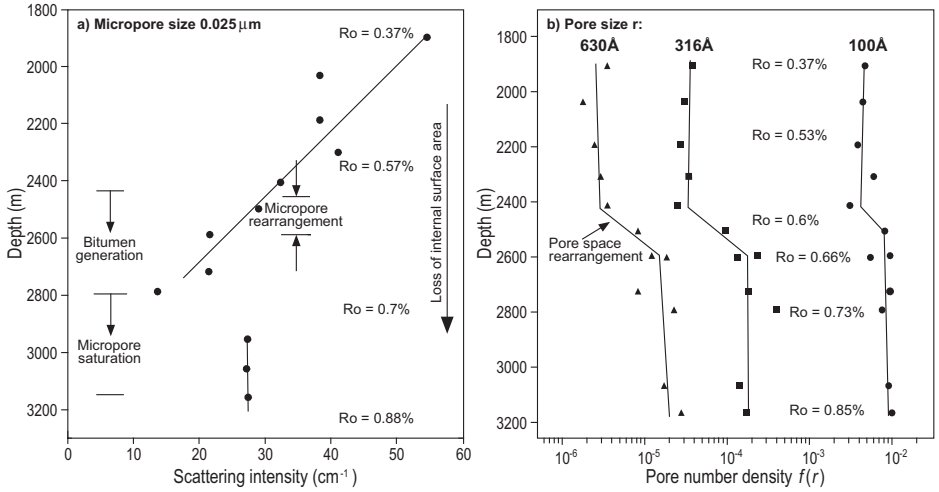

Figure 12. SANS results for coals from the Eastern View Sequence (Pelican-5 well, Bass Basin, Australia) showing (a) variation of the scattering intensity versus depth (for mean micropore size 25 nm ± 12 nm) and (b) pore number density calculated from SANS data using the PDSP model for micropore sizes 100, 316 and 630 Å (after Boreham et al. 2003).

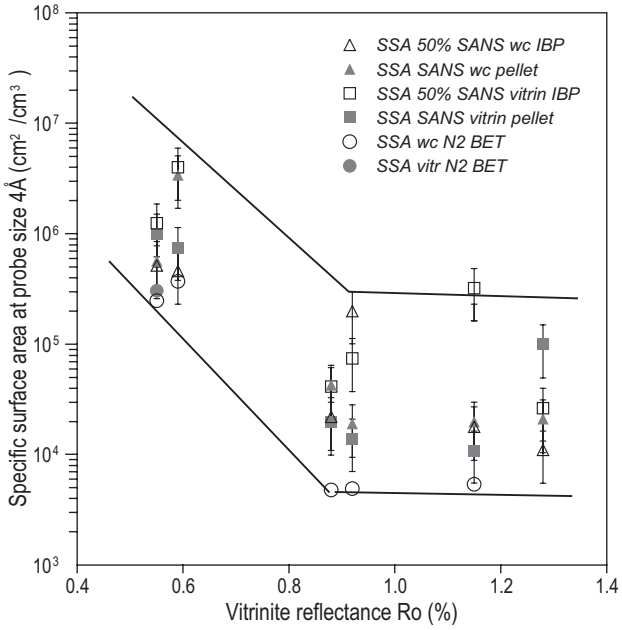

Figure 13. Comparison between specific surface area for coals of different ranks extrapolated to probe diameter 4 Å from SANS and nitrogen adsorption techniques.

by an independent method (Berkowitz 1979). The agreement is remarkably good and illustrates the utility of the PDSP model in interpreting SAS data for sedimentary rocks.

Igneous rocks and opals

Microstructure of igneous rocks. SANS work on igneous rocks was pioneered by Lucido et al. (1985). They studied alkaline basaltic rocks from Sicily and New Zealand and concluded that neutron scattering originated from light-colored small particles (leucocratic ocelli with an average diameter of around 190 Å) embedded in the rock—indicating the system had undergone rapid cooling near the critical condition. SANS data from a number of volcanic and plutonic rocks from South Africa, Morocco and Sardinia were interpreted as surface fractal scattering on droplets precipitated during spinodal decomposition of magma cooled at or near the critical condition (Lucido et al. 1988, 1991).

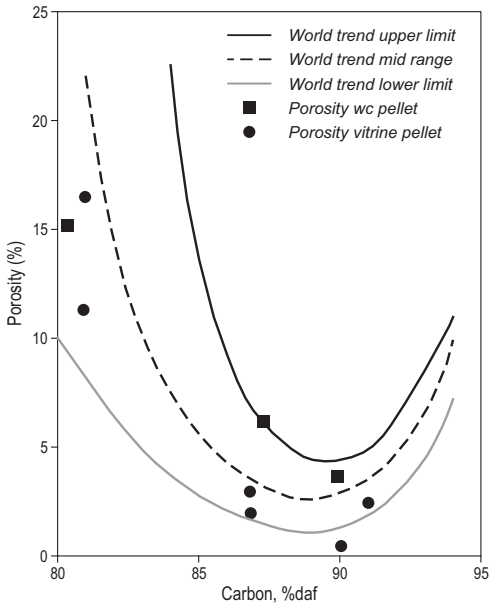

Figure 14. Porosity of coals and vitrinites calculated from SANS/USANS data for pore size range 2.5 nm to 10 μm (after Radlinski et al. 2004c).

Kahle et al. (2004) performed a combined SANS and microscopic study of various types of volcanic rocks: basalt, rhyolite, phonolitic pumice, phonolite and rhyolitic obsidian. Some of the rocks were thermally treated up to a temperature of 1900 K. The composition of samples was determined using microprobe and X-ray fluorescence analysis. The SANS patterns were fractal-like for basalt (due to voids with fractal surfaces) and Porod-like for pumice and phonolite (due to pores with smooth surfaces—except for thermally treated samples at length scales below 300 Å). The authors calculated specific surface area for these rocks and discussed the effect of heat treatment on rock microstructure. The results for pumice were consistent with the previous work of Floriano et al. (1994). For rhyolitic obsidian (which has no porosity) scattering occurs on crystalline precipitates of FeO embedded in the rock matrix. This matrix is composed predominantly of SiO_2 and Al_2O_3.

The work of Kahle et al. (2004) is significant as it combines a quantitative interpretation of absolutely calibrated SANS data with a verification of structural models using SEM, optical microscopy and microprobe analysis. Figure 15 shows SANS data for basalt samples obtained by melting basalt powder at 1400 K for 20 minutes (samples 8 and 9) and for 3 hours (samples 10 and 11). For samples thermally treated for 20 minutes, the scattering is very similar to SANS of as-received solid basalt samples and indicates a fractal structure ($D_s \approx 2.5$-2.7) over the length range from 50 Å to at least 3000 Å. For samples thermally treated for 3 hours, however, the scattering intensity decreases by roughly one order of magnitude. Slopes in the range –4.25 to –4.15 indicate the presence of a fuzzy rather than fractal interface. SEM images for the two types of samples (three different magnifications for each type) illustrate the loss of porosity upon heat treatment (Fig. 16). This type of work provides insights into the microstructural consequences of thermal processing of rocks in earth-interior-like conditions and complements the neutron imaging work of Kahle et al. (2004) (Winkler et al. 2005; also see Winkler 2006, this volume).

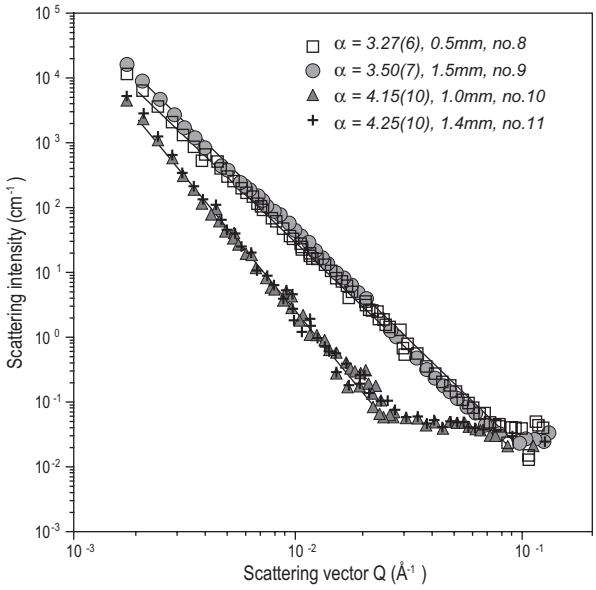

Figure 15. SANS data for 4 basalt samples thermally treated at 1400 K. Samples 8 and 9 were annealed for 20 minutes and samples 10 and 11 were annealed for 3 hours. [Reproduced with permission of E. Schweizerbart'sche Verlagsbuchhandlung (*http://www.schweizerbart.de,* from Kahle et al. (2004).]

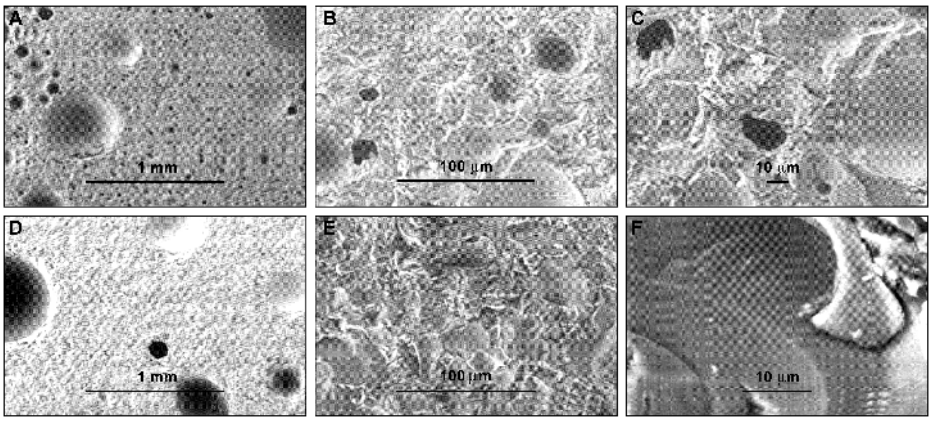

Figure 16. SEM images for basalt sample 8 (top) and sample 10 (bottom) showing the surface structure at various length scales. Magnification: A ×101, B ×1000, C ×1500, D ×100, E ×1010, F ×5000. [Reproduced with permission of E. Schweizerbart'sche Verlagsbuchhandlung (*http://www.schweizerbart.de,* from Kahle et al. (2004).]

Microstructure of opals. A precious opal of gem quality has been used for many years as a calibration standard for the D11 SANS facility at ILL (Ibel and Wright 1980). This particular application has led to a more extensive SANS study of a range of precious opals and potch opals from Australia, Brazil and Spain, as well as synthetic opals, flint nodules and a chalcedony band in an agate geode (Graetsch and Ibel 1997). Opals consist of closely packed

non-crystalline silica spheres, with interstices filled with water and non-crystalline silica cement. The authors relate the SANS scattering patterns for these minerals in the Porod region to the type of stacking, the size distribution of the silica spheres, the amount of intersitial water and the chemical composition of the cement. Chalcedony and flint are composed of submicroscopic quartz fibers, and their SANS patterns are distinctly different (they also exhibit significantly less incoherent background scattering than opal). Figure 17 illustrates the SANS spectra of microcrystalline opals and quartz minerals (flint and chalcedony).

Clays

Due to their importance in civil engineering and in drilling-mud used in exploration drilling, clay/water mixtures have been studied extensively (including microstructural investigations using SAXS and SANS). Critical issues in the study of clays are the permeation of water and associated clay-swelling. For example, a mixture of water and sodium montmorillonite (a smectite) can form a thixotropic gel composed of up to 10 g of water per gram of clay.

The building blocks of clay minerals are flat, hydrophilic platelets about 10 Å thick with diameters in the range of hundreds to thousands of Å. In an aqueous environment, the clay platelets form sheet-like stacked layers intercalated with aqueous regions (pores). Typical dimensions in water-clay mixtures range from 10 Å for the thickness of a single layer, tens to thousands of Å for repeatable packages of stacked layers to hundreds of Å to tens of micrometers for clay platelet diameters and pore sizes (Knudsen et al. 2003). In order to fully describe these structures it is usually necessary to acquire data in a Q-range combining SANS (SAXS) and USANS (USAXS).

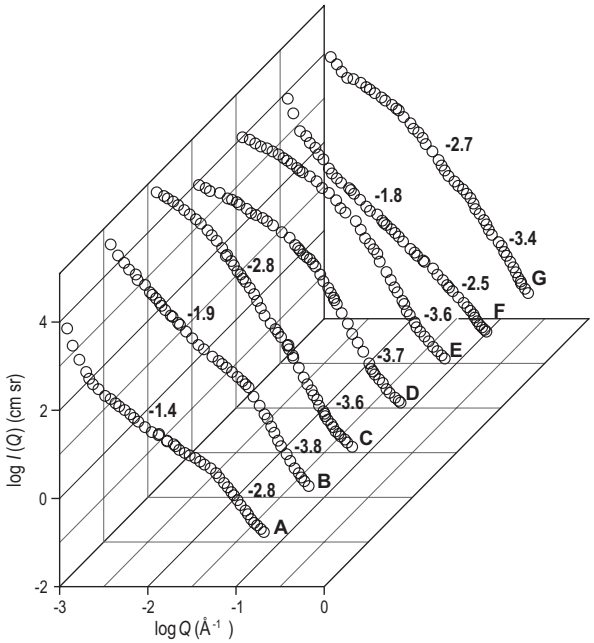

Figure 17. Radially averaged SANS data for microcrystalline opals and quartz minerals. A-C: opal-CT; D, E: opal-C; F: flint; G-chalcedony. Numbers refer to the slopes of the linear parts of the scattering curves. [Reproduced with kind permission of Springer Science and Business Media, from Graetsch and Ibel (1977)]

Morvan et al. (1994) reviewed early SANS and SAXS work on clays and presented results of SAXS and USAXS studies of suspensions of synthetic clay, laptonite (in water, up to 10% (w/w)) and of sodium montmorillonite clay (both in water (up to 20% (w/w) and in 1 M and 2 M NaCl (1.7% (w/w)). Figure 18 illustrates textures observed for montmorillonite samples dispersed in pure water and in brine and in swollen montmorillonite. Figure 19 shows calculated scattering curves for three different microstructures found in laptonite and montmorillonite.

Allen (1991) used SANS to test a microstructural model for compacted London clay and Oxford clay. His model is similar to that presented in Figure 18c, where the interlayer pores are called type I, pores between the closely inter-twined strands of lamellar stacks of different orientation are called type II and large, water containing pores are called type III. According to his analysis, type I pores are too small to be observed by SANS, a type II pore structure is a volume fractal and a type III pore surface is a surface fractal. Allen (1991) used the contrast-matching SANS method to observe swelling of London clay and Oxford clay and conjectured on the exchange of H_2O to D_2O in various pore types.

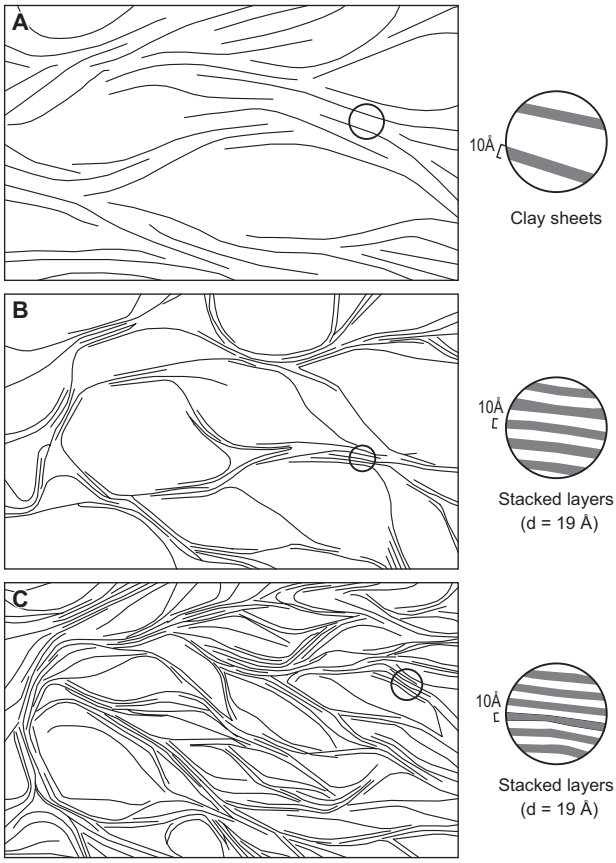

Figure 18. Three types of microstructural textures observed in montmorillonite clays. A: biphasic (nematic + holes), observed in sodium montmorillonite dispersed in pure water (Q^{-3} behavior at small Q-values); B: collapsed nematic + holes, observed in sample A after brine was added (Q^{-2} behavior at small Q-values); C: binding of dense sediments, observed in montmorillonite swollen in contact with brine (Q^{-3} behavior at small Q-values). [Reproduced from Morvan et al. (1994), with permission from Elsevier.]

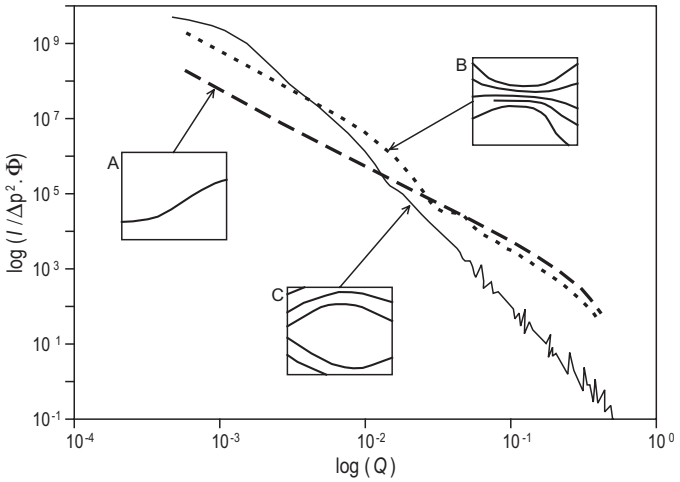

Figure 19. Small-angle scattering intensity (normalized to the contrast value, $\Delta\rho^2$, and clay volume fraction Φ) for three structural features in clays. A: water suspension of randomly oriented discs of radius 5000 Å and thickness 10 Å; B: water suspension of a mixture of randomly oriented discs of dimensions as in A and stacks of discs of radius 5000 Å and thickness 200 Å; C: polydisperse spherical pores filled with water in swollen clays. [Reproduced from Morvan et al. (1994), with permission from Elsevier.]

Knudsen et al. (2003) used SANS to obtain structural information about the synthetic clay Na-fluorohectorite. Oriented dehydrated samples (of porosity 41%) were prepared from suspension by applying uniaxial pressure (up to 26 MPa) at 120 °C. The microstructure of these samples at two orientations (parallel and perpendicular to applied stress) was assessed by SANS at various temperatures and water saturation. The obtained anisotropy ratio was 2:1, and the scattering curves were interpreted along the lines of a two-dimensional Debye model (Debye et al. 1957; Hall et al. 1983). Clay platelets were oriented preferentially in the direction perpendicular to applied stress. The relative pore water content in dry, normal and wet conditions was determined. The dynamics of water transport in a wet sample was studied using D_2O substitution and it was concluded that a slow restructuring of the internal surface may be taking place during H_2O/D_2O exchange on the time scale of about 10 hours.

Itakura et al. (2005) analyzed anisotropic multiple scattering USANS and SANS results obtained from two reconstituted samples of a natural kaolinitic soil used for containing industrial sludge waste. Samples were prepared from a slurry-like soil-water mixture uniaxially compressed at 400 kPa and 800 kPa. The authors demonstrate that the specific internal surface area obtained from multiple scattering analyses of water-saturated soils is consistent with the results of the Brunauer-Emmett-Teller (BET) method for air-dried fractions, thus providing a method for measuring the surface area of thick samples of fluid-saturated porous media.

MULTIPLE SCATTERING

The effect of multiple scattering on SANS curves

In the above we have assumed that each incident neutron has been scattered no more than once inside the specimen. In this approximation, the scattering cross section is independent of the neutron wavelength. Scattering, however, is a statistically random process and the probability of multiple scattering (MS) is finite but small (even for samples much thinner than the neutron mean free path). As shown in Figure 20, MS manifests itself as broadening

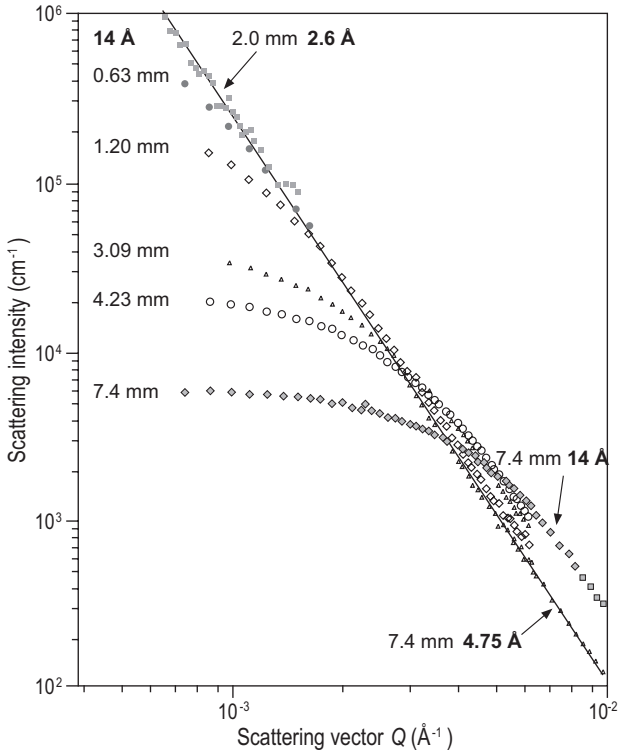

Figure 20. Multiple scattering SANS curves for a coarse sandstone measured using several neutron wavelengths for samples of various thicknesses. Note that distortion from the single scattering cross section (shown with solid line) is most accentuated for thick samples and long wavelengths (A.P. Radlinski and P. Lindner, unpublished).

(washing out) of the scattering curve. Its influence is particularly pronounced in strongly scattering materials such as rocks, clays, cements, ceramics, etc, for which the mean free path can be of the order of millimeters. The effect of MS is strongest in the small-Q region (for large scattering particle sizes) and MS probability depends on neutron wavelength as λ^2. Consequently, USANS and long wavelength SANS data for strongly scattering materials (including rocks) are susceptible to MS effects (Fig. 20).

In most cases, multiple scattering is an unwanted complication. A typical preventive approach is to prepare several samples of the same material of varying thicknesses to verify experimentally that there is no variation in the shape of the scattering curve (e.g., Radlinski et al. 1999). However, there is usually a practical limit to how thin a sample can be made. In some cases, SANS and USANS work is purposely undertaken on thick samples and the resulting MS patterns used to extract microstructural information.

Neutron scattering regimes

The formulation of neutron scattering regimes dates back to Weiss (1951) and has been more recently reviewed by Berk and Hardman-Rhyne (1988) and Krueger et al. (1991). The phase shift υ that a plane wave undergoes in traversing a scattering particle of radius R is $\upsilon = 2\Delta\rho R\lambda$, where $\Delta\rho = \rho_{particle} - \rho_{matrix}$ and ρ for each phase is given by Equation (25). Three scattering regimes are defined. The case of $\upsilon << 1$ is the usual SANS diffraction regime,

where the scattered intensity is described by the Born approximation. The opposite case of $\upsilon >> 1$ represents the multiple refraction regime, where the scattered intensity is derived from geometrical optics (von Nardroff 1926) and depends only upon the difference in index of refraction between the two phases (which itself is proportional to λ^2). Finally, the case of $\upsilon \approx 1$ is the MS regime most commonly encountered in SANS experiments for which the results can neither be described by a conventional SANS mechanism nor by multiple refraction.

SANS work utilizing multiple scattering (MS)

There have been a number of approaches to the MS problem. The literature is extensive and a non-exhaustive list of references is given. Weiss (1951) provided a general discussion and analysis of SANS data for several metallic powders and carbon black with a particle size of about 0.1 mm; Schelten and Schmatz (1980) derived analytical expressions (in kinematic approximation) for MS effects and calculated the single scattering cross section from MS patterns; Sabine and Bertram (1999) simplified the numerical scheme of Schelten and Schmatz and applied the theory to USANS data for a hydrated cement paste; Berk and others published a series of papers on MS theory and analysed SANS data for ceramics (Berk and Hardman-Rhyne 1986, 1988; Allen and Berk 1994); Mazumder and Sequeira (1992) worked on the theory of MS in statistical media; Krueger et al. (1991) applied MS to study the evolution of pore size distribution in alumina upon sintering; Maleyev (1995) considered theoretically MS from fractals; Bertram (1996) used computer simulations to investigate correlation effects in a system of closely packed polydispersed spheres; Šaroun (2000) developed a numerical scheme for MS USANS results and tested it on simulated data for polydispersed spheres; Bertram (2004) developed a method for extracting a single scattering differential cross section from MS USANS patterns based on matching Fourier transforms, which was subsequently applied to investigate the structure of oil-bearing and synthetic rock (Connolly et al. 2006).

NEUTRONS OR X-RAYS?

SANS and SAXS provide complementary information about the microstructure of rocks. Selection of a particular experimental technique should be based on careful analysis of the system to be studied, as the choice of neutrons or X-rays (or both) depends both on the type of rock and the microstructural problem at hand. Important issues to consider are the contrast, scale range of the inhomogeneities of interest, the sample size and the size of sample region to be investigated.

Neutrons have the ability to penetrate thick samples, offer a very wide range of scattering length density for contrast matching (or enhancement) and SANS data can be interpreted using a two-phase approximation for rocks with mixed organic-inorganic solid matrices. SAXS instruments offer high spectral resolution (small $\Delta\lambda/\lambda$) and can be used with small samples. SAXS data are unaffected by the incoherent scattering background. Synchrotron based SAXS instruments have a high beam intensity, which is very useful for low contrast samples. Some synchrotron-based SAXS instruments offer tight focus down to a 20 μm beam diameter.

CONCLUDING REMARKS

Collectively, modern SANS and USANS instruments provide access to microstructural features in rocks between 1 nm and 20 μm in size. Theoretical methods for reduction and interpretation of experimental data are well developed and numerous examples of applications are available in the literature. In recent years geological applications of SANS and USANS have matured to the point that they have became tools used to address geological questions rather than just a means to study individual rock samples.

Progress over the last two decades owes much to the theoretical advances made in relation to rock fractality, to the availability of absolutely calibrated SANS instruments and the development of a practical USANS instrument. With the proliferation of reactor based SANS and USANS instruments and the construction of new generation spallation neutron sources such as SNS, technological developments will play an important role in the future. For instance, the construction of a USANS instrument capable of detecting features up to 0.3 mm across is currently planned. Further developments in the use of grazing angle diffraction and reflectometry for studies of adsorbed molecules and the near-surface regions of rocks are possible.

The next frontier appears to be the ability to perform neutron scattering experiments at subsurface temperatures and pressures. High temperatures and pressures of the order of 100 GPa, characterize the Earth's lower mantle. These conditions can be replicated with laser-heated diamond anvil devices which hold very small volumes of rock. Such cells are currently being constructed for neutron scattering experiments at the new SNS facility (Parise 2006, this volume). Temperatures of up to 1300 °C and pressures up to 1 GPa (including a controlled axial component), simulating conditions down to a depth of approximately 50 km, are routinely used on large samples in rock physics experiments. A new field of study (*in situ* microstructural research in magmatic rocks) would present itself if these devices could be adapted to neutron diffraction and SANS experiments. A SANS cell capable of a maximum temperature of 400 °C and a pressure of 100 MPa would be sufficient to simulate conditions necessary to generate oil and gas from organic matter embedded in hydrocarbon source rocks and to study *in situ* the dynamics of hydrocarbon generation.

ACKNOWLEDGMENTS

Thanks are given to Steve Cadman and Alan Hinde for assistance in preparing this text and to J.S. Lin, D.R. Cole and H.R. Wenk for reviewing the manuscript. A.P. Radlinski publishes this chapter with the permission of the CEO, Geoscience Australia.

REFERENCES

Adler PM, Jacquin CG, Quiblier JA (1990) Flow in simulated porous media. Int J Multiphase Flow 16:691-712

Agamalian M, Wignall GD, Triolo R (1997) Optimization of a Bonse-Hart ultra-small-angle neutron scattering facility by elimination of the rocking-curve wings. J Appl Crystallogr 30:345-352

Allen AJ, Berk NF (1994) Analysis of small angle scattering data dominated by multiple scattering for systems containing eccentrically shaped particles or pores. J Appl Crystallogr 27:878-891

Allen AJ (1991) Time-resolved phenomena in cements, clays and porous rocks. J Appl Crystallogr 24:624-634

Auvray L, Auroy P (1991) Scattering by interfaces: variations on Porod's law. *In*: Neutron, X-ray and light scattering. Lindner P, Zemb Th (eds) Elsevier, p 199-221

Bale HD, Schmidt PW (1984) Small-angle X-ray scattering investigation of submicroscopic porosity with fractal properties. Phys Rev Lett 53:596-599

Berk NF, Hardman-Rhyne KA (1986) The phase shift and multiple scattering in small angle neutron scattering: application to beam broadening from ceramics. Physica B 136:218-222

Berk NF, Hardman-Rhyne KA (1988) Analysis of SAS data dominated by multiple scattering. J Appl Crystallogr 21:645-651

Berkowitz N (1979) An Introduction to Coal Technology. Academic Press

Bertram WK (1996) Correlation effects in small-angle neutron scattering from closely packed spheres. J Appl Crystallogr 29:682-685. See also Bertram WK (1988) Response to Pedersen's comment on 'Correlation effects in small-angle neutron scattering from closely packed spheres'. J Appl Crystallogr 31:489

Bertram WK (2004) Multiple scattering of USANS data using the method of matching Fourier transform. Presented at the Annual National Meeting of the American Crystallographic Association, Chicago 2004.

Bonse U, Hart M (1965) Small-angle X-ray scattering by spherical particles of polystyrene and polyvinyltoluene. Appl Phys Lett 7:238-240
Boreham CJ, Blevin JE, Radlinski AP, Trigg KR (2003) Coals as a source of oil and gas: a case study from the Bass Basin, Australia. Aust Pet Production Explor Assoc J 117-147
Broseta D, Barré L, Vizika O (2001) Capillary condensation in fractal porous medium. Phys Rev Lett 86: 5313-5316
Cohen MH (1987) The morphology of porous sedimentary rocks. *In*: Physics and chemistry of porous media II", AIP Conference Proceedings 154. Banavar JR, Koplik J, Winkler KW (eds) Am Inst Physics, p 1-16
Cole DR, Herwig KW, Mamontov E, Larese J (2006) Neutron scattering and diffraction studies of fluids and fluid-solid interactions. Rev Mineral Geochem 63:313-362
Connolly J, Bertram W, Barker J, Buckley C, Edwards T, Knott R (2006) Comparison of the structure on the nanoscale of natural oil-bearing and synthetic rock. J Petr Sci Eng 53(3-4):171-178
Debye P, Bueche AM (1949) Scattering by an inhomogeneous solid. J Appl Phys 20:518-525
Debye P, Anderson HR Jr, Brumberger H (1957) Scattering by an inhomogeneous solid. II. The correlation function and its application. J Appl Phys 28:679-683
Dianoux AJ, Lander G (eds) (2002) Neutron Data Booklet. Institut Laue-Langevin, Neutrons for Science
Espinat D (1990) Application des techniques de diffusion de la lumière, des rayons X et des neutrons à l'étude des systèmes colloïdaux. Rev l'Institut Français du Pétrole 45(6):1-131
Feigin LA, Svergun DI (1987) Structure Analysis by Small-angle X-ray and Neutron Scattering. Plenum Press
Floriano MA, Venezia AM, Deganello G, Svensson EC, Root JH (1994) The structure of pumice by neutron diffraction. J Appl Crystallogr 27:271-277
Freltoft T, Kjems JK, Sinha SK (1996) Power-law correlations andfinite-size effects in silica particle aggregates studied by small-angle neutron scattering. Phys Rev B 33:269-275
Glatter O, Kratky O (eds) (1982) Small Angle X-ray Scattering. Academic Press
Glinka CJ, Rowe JM, LaRock JG (1986) The small-angle neutron scattering spectrometer at the National Bureau of Standards. J Appl Crystallogr 19:427-439
Graetsch H, Ibel K (1997) Small angle neutron scattering of opals. Phys Chem Minerals 24:102-108
Guinier A, Fournet G, Walker CB, Yudowitch KL (1955) Small-angle Scattering of X-rays. John Wiley and Sons
Hainbuchner M, Villa M, Kroupa G, Bruckner G, Baron M, Amenitsch H, Seidl E, Rauch H (2000) The new high resolution ultra-small-angle neutron scattering instrument at the High Flux Reactor in Grenoble. J Appl Crystallogr 33:851-854
Hall PL, Mildner DFR, Borst RL (1983) Pore size distributions of shaly rock by small angle neutron scattering. Appl Phys Lett 43:252-254
Hansen JP, Skjeltrop AP (1988) Fractal pore space and rock permeability implications. Phys Rev B 38:2635-2638
Hinde AL (2004) PRINSAS – a Windows-based computer program for the processing and interpretation of small-angle scattering data tailored to the analysis of sedimentary rocks. J Appl Crystallogr 37:1020-1024
Ibel K, Wright A (1980) An opal standard for very low momentum transfers in neutron small angle scattering. ILL Internal Scientific Report 80IB45S
Ioannidis MA, Kwiecien MJ, Chatzis I (1996) Statistical analysis of the porous microstructure as a method of estimating reservoir permeability. J Pet Sci Eng 16:251-261
Itakura T, Bertram WK, Knott RB (2005) The nanoscale structural response of a natural kaolinitic clayey soil subjected to uniaxial compression. Appl Clay Sci 29:1-14
Jacquin CG, Adler PM (1987) Fractal porous media. II: Geometry of porous geological structures. Transp Porous Media 2:571-596
Johnston PR, McMahon P, Reich MH, Snook IK, Wagenfeld HK (1993) The effect of processing on the fractal pore structure of Victorian brown coal. J Coll Interf Sci 155:146-151
Kahle A, Winkler B, Radulescu A, Schreuer J (2004) Small-angle neutron scattering study of volcanic rocks. Eur J Mineral 16:407-417
Katz AJ, Thompson AH (1985) Fractal sandstone pores: implications for conductivity and pore formation. Phys Rev Lett 54:1325-1328
Knudsen KD, Fossum JO, Helgesen G, Bergaplass V (2003) Pore characteristics and water absorption in a synthetic smectite clay. J Appl Crystallogr 36:587-591
Koehler WC (1986) The national facility for small-angle neutron scattering. Physica B 137:320-329
Krishnamurti P (1930) Studies in X-ray diffraction. Part I: The structure of amorphous scattering. Part II: Colloidal solutions and liquid mixtures. Indian J Phys 5:473-500
Krohn CE (1988) Sandstone fractal and Euclidean pore volume distributions. J Geophys Res 93(B4):3286-3296

Krueger S, Long GG, Page RA (1991) Characterization of the densification of alumina by multiple small-angle neutron scattering. Acta Crystallogr A47:282-290
Lambard J, Zemb Th (1991) A triple-axis Bonse-Hart camera used for high-resolution small-angle scattering. J Appl Crystallogr 24:555-561
Letcher JR, Schmidt PW (1966) Small-angle x-ray scattering determination of particle-diameter distributions in poly-disperse suspensions of spherical particles. J Appl Phys 37:649-655
Li JC, Ross DK, Howe LD, Stefanopoulos KL, Fairclough JPA, Heenan R, Ibel K (1994a) Small-angle neutron scattering studies of the fractal-like network formed during desorption and adsorption of water in porous materials. Phys Rev B 49:5911-5917
Lin JS, Hendricks RW, Harris LA, Yust CS (1978) Microporosity and micromineralogy of vitrinite in a bituminous coal. J Appl Crystallogr 11:621-625
Lin MY, Sinha SK, Drake JM, Wu X-I, Thiyagarajan P, Stanley HB (1994b) Study of phase separation of binary fluid mixture in confined geometry. Phys Rev Lett 72:2207-2210
Lindner P, Zemb Th (eds) (1991) Neutron, X-ray and Light Scattering. Elsevier
Lindner P, May RP, Timmins PA (1992) Upgrading of the SANS instrument D11 at the ILL. Physica B 180&181:967-972
Lucido G, Caponetti E, Triolo R, (1985) Preliminary small-angle neutron scattering experiments on magmatic rocks to detect critical phenomena. Mineral Petrogr Acta XXIX:133-138
Lucido G, Triolo R, Caponetti E (1988) Fractal approach in petrology: Small-angle neutron scattering experiments with volcanic rocks. Phys Rev B 39:9742-9745
Lucido G, Caponetti E, Triolo R, (1991) Fractality as a working tool for petrology: small-angle neutron scattering experiments to detect critical behaviour of magma. Geologica Carpathica 42:85-91
Maleyev SV (1995) Small-angle neutron scattering in fractal media. Phys Rev B 52:13163-13168
Mandelbrot BB (1977) Fractals: Form, Chance and Dimension. Freeman
Mandelbrot BB (1982) The Fractal Geometry of Nature. Freeman
Martin JE, Hurd AJ (1987) Scattering from fractals. J Appl Crystallogr 20:61-78
Mazumder S, Sequeira A (1992) Multiple small-angle scattering from a statistical medium. J Appl Crystallogr 25:221-230
Mc Mahon PJ, Treimer W (1998) The geometric origin of asymmetric small angle neutron scattering from an elastically bent double crystal diffractometer. J Crystallogr Res Technol 33:625-636
McMahon PJ, Snook IK, Treimer W (2002) The pore structure in processed Victorian brown coal. J Coll Interf Sci 251:177-183
McMahon PJ, Snook I, Smith E (2001) An alternative derivation of the equation for small angle scattering from pores with fuzzy interfaces. J Chem Phys 114:8223-8225
Melnichenko YB, Wignall GD, Cole DR, Frielinghaus H, Bulavin LA (2005) Liquid-gas critical phenomena under confinement: small angle neutron scattering studies of CO_2 in aerogel. J Mol Liquids 120:7-9
Mikula P, Lukas P, Eichhorn F (1988) A new version of a medium-resolution double-crystal diffractometer for the study of small-angle neutron scattering (SANS). J Appl Crystallogr 21:33-37
Mildner DFR, Hall PL, (1986) Small-angle scattering from porous solids with fractal geometry. J Phys D Appl Phys 19:1535-1545
Morvan M, Espinat D, Lambard J, Zemb T (1994) Ultrasmall- and small-angle X-ray scattering of smectite clay suspensions. Colloids Surf A 82:193-203
von Nardroff R (1926) Refraction of X-rays by small particles. Phys Rev 28:240-246
Parise JB (2006) High pressure studies. Rev Mineral Geochem 63:205-231
Pfeifer P, Avnir D (1983) Chemistry of noninteger dimensions between two and three. I. Fractal theory of heterogeneous surface. J Chem Phys 79:3558-3565
Porod G (1951) Die Röntgenkleinwinkelstreuung von dichtgepackten kolloiden Systemen. I Teil. Kolloid Z 124:83-114
Porod G (1952) Die Röntgenkleinwinkelstreuung von dichtgepackten kolloiden Systemen. II Teil. Kolloid Z 125:51-57, 108-122
Porod G (1982) General Theory. *In*: Small angle X-ray scattering. Glatter O, Kratky O (eds) Academic Press, p 17-51
Prinz D, Pyckhout-Hintzen W, Littke R (2004) Development of meso- and macroporous structure of coals with rank as analysed with small angle neutron scattering and adsorption experiments. Fuel 83:547-556
Radlinski AP, Boreham CJ, Wignall GD, Lin JS (1996a) Microstructural evolution of source rocks during hydrocarbon generation: A small-angle scattering study. Phys Rev B 53:14152-14160
Radlinski AP, Barré L, Espinat D (1996b) Aggregation of n-alkanes in organic solvents. J Mol Structure 383: 51-56
Radlinski AP, Radlinska EZ, Agamalian M, Wignall GD, Lindner P, and Randl OG (1999) Fractal geometry of rocks. Phys Rev Lett 82:3078-3081

Radlinski AP, Radlinska EZ (1999) The microstructure of pore space in coals of different rank: a small angle scattering and SEM study. *In*: Coalbed Methane: Scientific, Environmental and Economic Evaluation. Mastalerz M, Glikson M, Golding SD (eds) Kluvier Scientific Publishers, p 329-365

Radlinski AP, Boreham CJ, Lindner P, Randl OG, Wignall GD, Hope JM (2000a) Small angle neutron scattering signature of oil generation in artificially and naturally matured hydrocarbon source rocks. Org Geochem 31:1-14

Radlinski AP, Radlinska EZ, Agamalian M, Wignall GD, Lindner P, and Randl OG (2000b) The fractal microstructure of ancient sedimentary rocks. J Appl Crystallogr 33:860-862

Radlinski AP, Hinde AL (2002) Small angle neutron scattering and petroleum geology. Neutron News 13: 10-14

Radlinski AP, Claoue-Long J, Hinde AL, Radlinska EZ, Lin JS (2003) Small angle X-ray scattering measurement of the internal micro-structure of natural zircon crystals. Phys Chem Minerals 30:631-640

Radlinski AP, Ioannidis MA, Hinde AL, Hainbuchner M, Baron M, Rauch H, Kline SR (2004a) Angstrom-to-millimeter characterization of sedimentary rock microstructure. J Colloid Interf Sci 274:607-612

Radlinski AP, Kennard JM, Edwards DS, Hinde AL, Davenport R (2004b) Hydrocarbon generation and expulsion from Early Cretaceous source rocks in the Browse Basin, North West Shelf, Australia: a SANS study. Aust Pet Production Explor Assoc J 2004:151-180

Radlinski AP, Mastalerz M, Hinde AL, Hainbuchner M, Rauch H, Baron M, Lin JS, Fan L, Thiyagarajan P (2004c) Application of SAXS and SANS in evaluation of porosity, pore size distribution and surface area of coal. Int J Coal Geology 59:245-271

Reich MH, Russo SP, Snook IK, Wagenfield HK (1990) The application of SAXS to determine the fractal properties of porous carbon-based materials. J Colloid Interface Sci 135:353-362

Russell TP, Lin JS, Spooner S, Wignall GD (1988) Intercalibration of small-angle X-ray and neutron scattering data. J Appl Crystallogr 21:629-638

Sabine TM, Bertram WK (1999) The use of multiple-scattering data to enhance small-angle neutron scattering experiments. Acta Crystallogr A55:500-507

Šaroun J (2000) Evaluation of double-crystal SANS data influenced by multiple scattering. J Appl Crystallogr 33:824-828

Schaefer DW, Keefer KD (1984) Fractal geometry of silica condensation polymers. Phys Rev Lett 53:1383-1386

Schaefer DW, Wilcoxon JP, Keefer KD, Bunker BC, Pearson RK, Thomas IM, Miller DE (1987) Origin of porosity in synthetic materials. *In*: Physics and chemistry of porous media II", AIP Conference Proceedings 154, Banavar JR, Koplik J, Winkler KW (eds) Am Inst Physics, p 63-80

Schelten J, Schmatz W (1980) Multiple-scattering treatment for small-angle scattering problems. J Appl Crystallogr 13:385-390

Schmidt PW (1982) Interpretation of small-angle scattering curves proportional to a negative power of the scattering vector. J Appl Crystallogr 15:567-569

Schmidt PW (1989) Use of scattering to determine the fractal dimension. *In*: The fractal approach to heterogeneous chemistry. Avnir D (ed) John Wiley and Sons, p 67-79

Schmidt PW, Avnir D, Levy D, Hohr A, Steiner M, Roll A (1991) Small angle x-ray scattering from the surfaces of reversed phase silicas: power-law scattering exponents of magnitudes greater than four. J Chem Phys 94:1474-1479

Sears VF (1990) Coherent neutron scattering amplitudes. *In*: Neutron Scattering at the High Flux Isotope Reactor. Mook HA, Nicklow RM (eds) Oak Ridge National Laboratory, p 29-30

Snook I, Yarovsky I, Hanley HJM, Lin MY, Mainwaring D, Rogers H, Zulli P (2002) Characterization of metallurgical chars by small angle neutron scattering. Energy Fuels 16:1009-1015

Spalla O, Lyonnard S, Testard F (2003) Analysis of the small-angle intensity scattered by a porous and granular medium. J Appl Crystallogr 36:338-347

Teixeira J (1988) Small-angle scattering by fractal systems. J Appl Crystallogr 21:781-785

Thiyagarajan P, Epperson JE, Crawford RK, Carpenter JM, Klippert TE, Wozniak DG (1997) The time-of-flight small angle neutron diffractometer (SAD) at IPNS, Argonne National Laboratory. J Appl Crystallogr 30:280-293

Thompson AH (1991) Fractals in rock physics. Annu Rev Earth Planet Sci 19:237-262

Vacher R, Woignier T, Peloue J, Courtens E (1988) Structure and self-similarity of silica aerogels. Phys Rev B 37:6500-6503

Vogel SC, Priesmeyer H-G (2006) Neutron production, neutron facilities and neutron instrumentation. Rev Mineral Geochem 63:27-57

Warren BE (1934) X-ray diffraction study of carbon black. J Chem Phys 2:551-555

Weiss RJ (1951) Small angle scattering of neutrons. Phys Rev B 83:379-389

Wignall GD, Bates FS (1987) Absolute calibration of small-angle neutron scattering data. J Appl Crystallogr 20:28-40

Winans RE, Thiyagarajan P (1988) Characterization of solvent-swollen coal by SANS. Energy Fuels 2:356-358

Winkler B (2006) Applications of neutron radiography and neutron tomography. Rev Mineral Geochem 63: 459-471

Winkler B, Kahle A, Hennion B (2006) Neutron radiography of rocks and melts. International Conference on Neutron Scattering, Sydney, November 2005. Physica B (in press)

Wong Pz, Howard J, Lin JS (1986) Surface roughening and the fractal nature of rocks. Phys Rev Lett 57: 637-640

Wong Pz, Bray AJ (1988) Porod scattering from fractal surfaces. Phys Rev Lett 60:1344

Wong Pz (2006) Studies of the fractal nature of sedimentary rocks by small angle scattering and other techniques. International Conference on Neutron Scattering, Sydney, Australia, November 2005. Physica B (in press)